



### 저작자표시-비영리-변경금지 2.0 대한민국

이용자는 아래의 조건을 따르는 경우에 한하여 자유롭게

- 이 저작물을 복제, 배포, 전송, 전시, 공연 및 방송할 수 있습니다.

다음과 같은 조건을 따라야 합니다:



저작자표시. 귀하는 원 저작자를 표시하여야 합니다.



비영리. 귀하는 이 저작물을 영리 목적으로 이용할 수 없습니다.



변경금지. 귀하는 이 저작물을 개작, 변형 또는 가공할 수 없습니다.

- 귀하는, 이 저작물의 재이용이나 배포의 경우, 이 저작물에 적용된 이용허락조건을 명확하게 나타내어야 합니다.
- 저작권자로부터 별도의 허가를 받으면 이러한 조건들은 적용되지 않습니다.

저작권법에 따른 이용자의 권리와 책임은 위의 내용에 의하여 영향을 받지 않습니다.

이것은 [이용허락규약\(Legal Code\)](#)을 이해하기 쉽게 요약한 것입니다.

[Disclaimer](#)



이학석사 학위논문

Study on Interaction of  
Air Composing Molecules and  
Lithium on Graphene Nanoflake by  
Density Functional Theory

밀도범함수 이론을 통한 그래핀 나노플레이크에서의  
공기 구성 분자와 리튬의 상호작용 연구

2021년 8월

서울대학교 대학원

화학부 물리화학 전공

신 채 수



Study on Interaction of  
Air Composing Molecules and  
Lithium on Graphene Nanoflake by  
Density Functional Theory

밀도범함수 이론을 통한 그래핀 나노플레이크에서의  
공기 구성 분자와 리튬의 상호작용 연구

지도 교수 신석민

이 논문을 이학석사 학위논문으로 제출함  
2021년 8월

서울대학교 대학원  
화학부 물리화학 전공  
신채수

신채수의 이학석사 학위논문을 인준함  
2021년 7월

위원장 정연준

부위원장 신석민

위원 석차옥



## Abstract

# Study on Interaction of Air Composing Molecules and Lithium on Graphene Nanoflake by Density Functional Theory

Chaesoo Shin

Physical Chemistry, Department of Chemistry

The Graduate School

Seoul National University

The advent of graphene, whose impact was recognized by the Nobel Prize in Physics in 2010, has garnered enormous attention to its wide applicability as electronics, light processing devices, new–property–materials, and 2D surface chemistry. The main interest in graphene includes its surface interaction with other chemical entities for catalysis, sensing, and storage. Especially, the Li doped graphene system has been related to various storage devices for energy purpose, for instance, Li storage, H<sub>2</sub> storage, and Li–air battery. The evaluation of effects of air molecules onto graphene–lithium system is essential to practical application for these purposes.

From the viewpoint of chemistry, to investigate the property and the application of graphene and graphene–like materials, approach from computational perspectives has been accepted. Such theoretical study has widely employed density functional theory to study various systems, for example, surface and edge of graphene, distinctive graphene–like materials, and energy storage applications.

Particularly, the Li–air battery system has been directly simulated, but its interaction with air is still not fully highlighted.

In this thesis, the interaction between air molecules and Li/Li<sup>+</sup> on graphene nanoflake was studied to elucidate its characteristics, using density functional theory. In Chapter 1, the motivation and necessity of this work will be suggested. In Chapter 2, background knowledge, especially about computational chemistry with density functional theory and graphene will be introduced. Previous study on property and application of graphene, and computational research on graphene will be also discussed.

In Chapter 3, computational methods in this study will be described in detail, and in Chapter 4, the results of the calculations will be explained. The role of Li/Li<sup>+</sup> was realization of the binding of Ar, N<sub>2</sub>, and O<sub>2</sub>. During the binding, the spin state of O<sub>2</sub> was revealed as triplet state. The binding structure of air molecules resembled the solvation shell structure, and the molecules and Li/Li<sup>+</sup> directly interacted only in the first shell. Unlike Ar, N<sub>2</sub> and O<sub>2</sub> showed linear end-on structure and bent end-on structure, respectively, with orientational effects. The charge of Li/Li<sup>+</sup> was found to be close to 1, indicating charge transfer for the neutral system. The average binding energy was converged because the stepwise binding energy was rather small and nearly constant in the second and the third shell. The unstable vibrational mode accompanying imaginary frequency limited the growth of the binding structure. The dispersion effects were prominent at the interaction of air molecules.

In Chapter 5, the discussion including comparison with H<sub>2</sub> and several comments will be proposed. Finally, in Chapter 6, the study in this work will be concluded. From this study, it was revealed that air can weaken H<sub>2</sub> storage capacity. Furthermore, Li doped graphene electrode could be damaged by excess N<sub>2</sub> or O<sub>2</sub>.

**Keyword:** density functional theory, graphene, graphene nanoflake, lithium, air, ambient condition

**Student Number:** 2015–20388

# Table of Contents

Chapter 1. Introduction .....	1
Chapter 2. Theoretical Background.....	3
2.1. Computational Chemistry .....	3
2.1.1. Electronic Structure of Molecules .....	3
2.1.2. Hartree–Fock Method .....	5
2.1.3. Density Functional Theory .....	6
2.1.4. Ab Initio and in Silico .....	9
2.1.5. Molecular Structure and Property .....	9
2.2. Graphene.....	10
2.2.1. Characteristics and Applications of Graphene ....	10
2.2.2. Computational Research on Graphene .....	11
Chapter 3. Computational Details .....	12
3.1. Simulations of Binding Mechanism of Air Molecules to Graphene–Lithium System .....	12
3.2. Quantitative Details of the Method.....	13
3.3. Effects of Several Relevant Factors to the Binding Mechanism .....	13
Chapter 4. Results.....	15
4.1. Reproducibility .....	15
4.2. Effects of Li/Li <sup>+</sup> to Binding Mechanism .....	15
4.3. Effects of Spin State of O <sub>2</sub> to Binding Mechanism ....	17
4.4. Binding Structures of Ar/N <sub>2</sub> /O <sub>2</sub> to GR(37)–Li/Li <sup>+</sup> ....	18
4.4.1. Ar on GR(37)–Li/Li <sup>+</sup> .....	18
4.4.2. N <sub>2</sub> on GR(37)–Li/Li <sup>+</sup> .....	23
4.4.3. O <sub>2</sub> on GR(37)–Li/Li <sup>+</sup> .....	27
4.5. Charge of Li/Li <sup>+</sup> and GR(37).....	31
4.6. Height of Li/Li <sup>+</sup> from GR(37) .....	32
4.6.1. Analysis with Local Charge of the Central Ring .	32
4.6.2. Analysis with Total Charge of the GR(37) .....	33
4.7. Binding Energy of Ar/N <sub>2</sub> /O <sub>2</sub> to GR(37)–Li/Li <sup>+</sup> .....	34
4.7.1. Effects of GR(37) to Binding of Ar/N <sub>2</sub> /O <sub>2</sub> to Li/Li <sup>+</sup> .....	35
4.8. Stability of GR(37)–Li/Li <sup>+</sup> –A <sub>n</sub> .....	36
4.9. Effects of Dispersion Corrections.....	36

Chapter 5. Discussion .....	43
5.1. Comparison with Previous Study on H <sub>2</sub> .....	43
5.2. Additional Comments.....	43
Chapter 6. Conclusions .....	44
 Bibliography .....	45
초록 .....	50
감사의 말.....	52

# Chapter 1. Introduction

Chemistry, the science about reaction between substances, has been progressed to elucidate reactivity and property of various substances. Thanks to the advancement of knowledge on chemistry, the behavior of substance can be grasped and predicted. By the knowledge about chemical behavior, understanding of the nature has been widened and the life of human has been enriched.

Such chemical activities involve small systems like molecules, ions, and lattices, so quantum mechanics has been employed to describe them.<sup>1</sup> Due to the growth of computer science, these quantum chemical systems can be computationally solved to give quantitative results for predicting many properties.<sup>2</sup> Since it is efficient approach that using the computational chemistry to the research, chemists actively adopted the method to reveal the property of target system like organic reactions, inorganic lattices, and 2D materials.

For example, graphene is an ongoing topic of such research. The advent of graphene<sup>3</sup> attracted great attention because of its remarkable electronic,<sup>4</sup> optical,<sup>5</sup> thermal,<sup>5</sup> mechanical,<sup>6</sup> and chemical<sup>7</sup> property, so it has been widely explored by scientists for its interesting applications. In particular, the application for energy device<sup>8</sup> is one of the key parts, and its surface interaction involving lithium species for Li storage,<sup>7–10</sup> H<sub>2</sub> storage,<sup>8, 11–13</sup> and Li–air battery<sup>14–18</sup> has been widely studied by experimental and theoretical methods. Although various computational approaches were attempted, to successfully achieve these purposes, evaluation of interaction between graphene–lithium system with air should be inevitably supplemented.<sup>15</sup>

In this thesis, interaction between air–composing molecules and Li species on graphene nanoflake surface was computationally studied to give intuition for practical purposes. Binding properties like structure, charge, energy parameter, and stability were analyzed. Not only comparison with H<sub>2</sub>, but also evaluation for practical application

was conducted. All works were performed with room temperature and pressure in mind.

# Chapter 2. Theoretical Background

## 2.1. Computational Chemistry<sup>19, 20</sup>

### 2.1.1. Electronic Structure of Molecules

In small system like molecule, due to the uncertainty principle, the position and the momentum are not proper physical quantities.

$$\sigma_x \sigma_p \geq \frac{\hbar}{2} \quad (2.1)$$

However, the law of energy conservation is always true, so energy is introduced to describe the quantum system by the Schrödinger equation.

$$\hat{H}\psi = E\psi \quad (2.2)$$

In the same vein as the matter wave, the wavefunction is used for the probability density  $|\psi|^2$ . Energy is obtained from the eigenvalue of the Hamiltonian operator  $\hat{H}$ .

Fundamentally, energy has its own operator. Besides, quantum system relies on its potential energy, so the Hamiltonian follows the expression for mechanical energy. Thus, the final form of the quantum mechanical description of a particle is

$$i\hbar \frac{\partial}{\partial t} \Psi(\vec{r}, t) = \left( -\frac{\hbar^2}{2m} \nabla^2 + V(\vec{r}) \right) \Psi(\vec{r}, t) \quad (2.3)$$

Normally it can be solved by separation of variables.

As the number of particles increases, the mathematical description becomes more complicate. In case of a molecule consisted of  $N$  nuclei and  $n$  electrons,

$$i\hbar \frac{\partial}{\partial t} \Psi(\underline{\vec{R}}, \underline{\vec{r}}, t) = \left( -\frac{\hbar^2}{2} \sum_{\alpha=1}^N \frac{1}{M_\alpha} \nabla_\alpha^2 - \frac{\hbar^2}{2m_e} \sum_{i=1}^n \nabla_i^2 + \frac{e^2}{4\pi\epsilon_0} \sum_{\alpha=1}^N \sum_{\beta>\alpha}^N \frac{Z_\alpha Z_\beta}{|\vec{R}_\alpha - \vec{R}_\beta|} \right. \\ \left. - \frac{e^2}{4\pi\epsilon_0} \sum_{\alpha=1}^N \sum_{i=1}^n \frac{Z_\alpha}{|\vec{R}_\alpha - \vec{r}_i|} + \frac{e^2}{4\pi\epsilon_0} \sum_{i=1}^n \sum_{j>i}^n \frac{1}{|\vec{r}_i - \vec{r}_j|} \right) \Psi(\underline{\vec{R}}, \underline{\vec{r}}, t) \quad (2.4)$$

is corresponding description, where  $\alpha$  and  $\beta$  refer to nuclei and  $i$  and  $j$  refer to electrons. In detail,  $M_\alpha$  is the mass of  $\alpha$ th nucleus,  $m_e$  is the mass of electron,  $Z_\alpha$  is the atomic number of  $\alpha$ th nucleus,  $\vec{R}_\alpha$  is the position of  $\alpha$ th nucleus,  $\vec{r}_i$  is the position of  $i$ th electron,  $\underline{\vec{R}} = \{\vec{R}_\alpha\}$ , and  $\underline{\vec{r}} = \{\vec{r}_i\}$ . The last term of right side shows interelectronic repulsion, and it makes the equation inseparable and insoluble.

To get the answer of the insoluble equation (2.4), we simplify the equation by several proper approximations. First, we can accept the adiabatic approximation, that is the system follows its configuration and maintains its eigenstate, if no sudden perturbation exists. Thus, electrons instantaneously follow nuclei, in practical process. Second, Born–Oppenheimer approximation is widely accepted, that is electrons move much faster than nuclei, so their movements can be treated separately.

By these, the wavefunction can be approximated as

$$\Psi(\underline{\vec{R}}, \underline{\vec{r}}, t) = \sum_{i=1}^n \theta_i(\underline{\vec{R}}, t) \phi_i(\underline{\vec{r}}; \underline{\vec{R}}) \quad (2.5)$$

where  $\theta$  refers wavefunction of nuclei and  $\phi$  refers wavefunction of electrons.

With (2.5) and given fixed nuclear coordinate  $\underline{\vec{R}}$ , purely electronic Hamiltonian can be constructed from (2.4) like

$$\widehat{H}_{el} = -\frac{\hbar^2}{2m_e} \sum_{i=1}^n \nabla_i^2 - \frac{e^2}{4\pi\epsilon_0} \sum_{\alpha=1}^N \sum_{i=1}^n \frac{Z_\alpha}{|\vec{R}_\alpha - \vec{r}_i|} + \frac{e^2}{4\pi\epsilon_0} \sum_{i=1}^n \sum_{j>i}^n \frac{1}{|\vec{r}_i - \vec{r}_j|} \quad (2.6)$$

with the purely electronic Schrödinger equation

$$\widehat{H_{el}}\phi_i(\underline{\vec{r}}; \underline{\vec{R}}) = E_i(\underline{\vec{R}})\phi_i(\underline{\vec{r}}; \underline{\vec{R}}) \quad (2.7)$$

Solving (2.7) is the first step to predict molecular chemical property. To solve it, we can follow one of two below representative methods.

### 2.1.2. Hartree–Fock Method

The Hartree–Fock method assumes the total electronic wavefunction as a product of  $n$  one-electron wavefunction with antisymmetric spin property and indistinguishability, so

$$\phi_{HF}(\underline{\vec{p}}) = \frac{1}{\sqrt{n!}} \begin{vmatrix} \phi_1(\vec{p}_1) & \phi_2(\vec{p}_1) & \dots & \phi_n(\vec{p}_1) \\ \phi_1(\vec{p}_2) & \phi_2(\vec{p}_2) & \dots & \phi_n(\vec{p}_2) \\ \vdots & \vdots & \ddots & \vdots \\ \phi_1(\vec{p}_n) & \phi_2(\vec{p}_n) & \dots & \phi_n(\vec{p}_n) \end{vmatrix} \quad (2.8)$$

where  $\underline{\vec{p}} = \{\vec{p}_i\}$ ,  $\vec{p}_i = (\vec{r}_i, S_i)$ , and  $S_i$  is the spin state of  $i$ th electron. Like (2.8), to consider all  $n$  electrons during energy calculation, (2.7) can be modified like below.

$$\begin{aligned} E_{HF} &= \langle \phi_{HF} | \widehat{H_{el}} | \phi_{HF} \rangle \\ &= -\frac{\hbar^2}{2m_e} \sum_{i=1}^n \int \phi_i^*(\vec{p}) \nabla_i^2 \phi_i(\vec{p}) d\vec{r} - \frac{e^2}{4\pi\epsilon_0} \sum_{\alpha=1}^N \sum_{i=1}^n \int \phi_i^*(\vec{p}) \frac{Z_\alpha}{|\vec{R}_\alpha - \vec{r}_i|} \phi_i(\vec{p}) d\vec{r} \\ &\quad + \frac{e^2}{4\pi\epsilon_0} \sum_{i=1}^n \sum_{j>i}^n \left( \iint \phi_i^*(\vec{p}_1) \phi_j^*(\vec{p}_2) \frac{1}{|\vec{r}_i - \vec{r}_j|} \phi_i(\vec{p}_1) \phi_j(\vec{p}_2) d\vec{r}_1 d\vec{r}_2 \right. \\ &\quad \left. - \delta_{S_i S_j} \iint \phi_i^*(\vec{p}_1) \phi_j^*(\vec{p}_2) \frac{1}{|\vec{r}_i - \vec{r}_j|} \phi_j(\vec{p}_1) \phi_i(\vec{p}_2) d\vec{r}_1 d\vec{r}_2 \right) \end{aligned} \quad (2.9)$$

From this, one electron equation can be constructed.

$$\begin{aligned} &\left( -\frac{\hbar^2}{2m_e} \nabla^2 - \frac{e^2}{4\pi\epsilon_0} \sum_{\alpha=1}^N \frac{Z_\alpha}{|\vec{R}_\alpha - \vec{r}_i|} + \frac{e^2}{4\pi\epsilon_0} \sum_{j=1}^n \int \frac{|\phi_j(\vec{p}_2)|^2}{|\vec{r}_i - \vec{r}_j|} d\vec{r}_2 \right) \phi_i(\vec{r}_1) \\ &+ \left( -\delta_{S_i S_j} \frac{e^2}{4\pi\epsilon_0} \sum_{j=1}^n \int \frac{\phi_j^*(\vec{p}_2) \phi_i(\vec{p}_2)}{|\vec{r}_i - \vec{r}_j|} d\vec{r}_2 \right) \phi_j(\vec{r}_1) = E_i \phi_i(\vec{r}_1) \end{aligned} \quad (2.10)$$

In the left side, the first integral term is Coulomb integral, and the second integral term is exchange integral. Fock operator  $\hat{F}$  can be introduced to (2.10), then similarly (2.7), it becomes the Hartree–Fock equation.

$$\hat{F}_1 \phi_i(\vec{r}_1) = \varepsilon_i \phi_i(\vec{r}_1) \quad (2.11)$$

With proper basis function,

$$\phi_i = \sum_{l=1}^L c_{li} \chi_l \quad (2.12)$$

we can get the (Hartree–Fock–)Roothaan equation

$$\sum_{l=1}^L c_{li} (\langle \chi_l | \hat{F} | \chi_l \rangle - \varepsilon_i \langle \chi_l | \chi_l \rangle) = 0 \quad (2.13)$$

and a secular equation.

$$\det(\langle \chi_l | \hat{F} | \chi_l \rangle - \varepsilon_i \langle \chi_l | \chi_l \rangle) = 0 \quad (2.14)$$

Solving this equation will give the electronic structure. Since  $\hat{F}$  depends on  $\phi_i$ , it must be solved by iteratively. Due to the variational principle, the lower energy means the better result. Generally, this method takes time proportional to  $n^4$ .

### 2.1.3. Density Functional Theory

The density functional theory (DFT) attempts to get electron density rather than wavefunction, which has lesser variables so easier to get,

$$\rho(\vec{r}) = n \int \cdots \int |\phi(\vec{r})| d\vec{r}_2 \cdots d\vec{r}_n \quad (2.15)$$

where  $\rho(\vec{r})$  is electron density. The electronic energy is expressed as functional of electron density, so  $E[\rho(\vec{r})]$ . By the Hohenberg–Kohn theorem, for ground state, denoted by 0,

1.  $\rho_0(\vec{r})$  determines  $n$  and  $V_0(\vec{r}_i) + C$  uniquely.<sup>①</sup>
2.  $E_0[\rho(\vec{r})]$  gives the lowest energy value if and only if the input density is  $\rho_0(\vec{r})$ .

where  $C$  is a constant and

$$V(\vec{r}_i) = \frac{e^2}{4\pi\varepsilon_0} \sum_{\alpha=1}^N \frac{Z_\alpha}{|\vec{R}_\alpha - \vec{r}_i|} \quad (2.16)$$

Due to this theorem,  $\rho_0(\vec{r})$  determines  $V_0(\vec{r}_i)$ , so we can get the  $\underline{\vec{R}}$  and the purely electronic Hamiltonian (2.6). This will give a  $\phi(\vec{r})$  corresponding to the  $\rho_0(\vec{r})$ . Therefore,  $\rho_0(\vec{r})$ ,  $V_0(\vec{r}_i)$ ,  $\widehat{H}_{el}$ , and  $\phi(\vec{r})$  are equivalent, and  $\rho_0(\vec{r})$  is a good alternative of  $\phi(\vec{r})$ .

Based on the result, we can conceive fictitious noninteracting electrons giving  $\rho_0(\vec{r})$ , then the wavefunction of (2.15) becomes

$$\phi(\underline{\vec{p}}) = \left| \prod_{i=1}^n \phi_i(\vec{p}_i) \right| \quad (2.17)$$

and

$$\rho_0(\vec{r}) = \sum_{i=1}^n |\phi_i(\vec{r})|^2 \quad (2.18)$$

For the electron density, (2.7) can be modified like

<sup>①</sup> In case of relationship between  $\rho_0(\vec{r})$  and  $V_0(\vec{r}_i)$ , it can be easily proved by the variational principle.

$$\begin{aligned}
& -\frac{\hbar^2}{2m_e} \sum_{i=1}^n \langle \phi_i(\vec{r}_1) | \nabla_1^2 | \phi_i(\vec{r}_1) \rangle - \frac{e^2}{4\pi\epsilon_0} \sum_{\alpha=1}^N Z_\alpha \int \frac{\rho(\vec{r}_1)}{|R_\alpha - \vec{r}_1|} d\vec{r}_1 \\
& + \frac{1}{2} \left( \frac{e^2}{4\pi\epsilon_0} \iint \frac{\rho(\vec{r}_1)\rho(\vec{r}_2)}{|\vec{r}_1 - \vec{r}_2|} d\vec{r}_1 d\vec{r}_2 \right) + E_{XC}[\rho_0(\vec{r})] = E_0[\rho_0(\vec{r})]
\end{aligned} \quad (2.19)$$

where  $E_{XC}[\rho]$  is exchange–correlation energy functional, and it is approximative term. From this, one electron equation can be constructed.

$$\begin{aligned}
& \left( -\frac{\hbar^2}{2m_e} \nabla_1^2 - \frac{e^2}{4\pi\epsilon_0} \sum_{\alpha=1}^N \frac{Z_\alpha}{|R_\alpha - \vec{r}_1|} + \frac{e^2}{4\pi\epsilon_0} \int \frac{\rho(\vec{r}_2)}{|\vec{r}_1 - \vec{r}_2|} d\vec{r}_2 \right. \\
& \left. + \frac{\delta E_{XC}[\rho_0(\vec{r})]}{\delta \rho_0(\vec{r})} \right) \phi_i(\vec{r}_1) = E_i \phi_i(\vec{r}_1)
\end{aligned} \quad (2.20)$$

In left side, last term shows the exchange–correlation potential.

$$V_{XC}(\vec{r}) = \frac{\delta E_{XC}[\rho_0(\vec{r})]}{\delta \rho_0(\vec{r})} \quad (2.21)$$

$V_{XC}(\vec{r})$  is still a major research topic of scientists,<sup>21</sup> but some approximations are widely accepted. According to the local density approximation (LDA),  $E_{XC}$  at some location only depends on the density of the location. Furthermore, by the generalized gradient approximation (GGA), gradient of density is used to correct variation of density away from the location. Kohn–Sham Hamiltonian  $\widehat{h_{KS}}$  can be introduced to (2.20), then similarly (2.7), it becomes the Kohn–Sham equation.

$$\widehat{h_{KS}} \phi_i(\vec{r}_1) = \varepsilon_i \phi_i(\vec{r}_1) \quad (2.22)$$

With proper basis function (2.12), we can get

$$\sum_{l=1}^L c_{li} (\langle \chi_\lambda | \widehat{h_{KS}} | \chi_l \rangle - \varepsilon_i \langle \chi_\lambda | \chi_l \rangle) = 0 \quad (2.23)$$

which resembles (2.13), and the secular equation analogous to (2.14) can be derived. Because  $\widehat{h_{KS}}$  depends on  $\phi_i$ , it will be solved by iteratively to give the electronic structure with lowest  $E_0$ . Generally, the time proportional to  $n^3$  is required to this method.

#### 2.1.4. Ab Initio and in Silico

Solving (2.13) or (2.23) by iteratively, we can get  $\chi_l$  to construct  $\phi_i$  of (2.12), so the solution of (2.7) is obtained. The suggested above methods use only physical constants to solve Hamiltonian. Therefore, these calculations are called a first principles calculation, or an ab initio calculation.<sup>②③</sup> They require lots of effort, so the works are performed by computer resources with proper simulation software, in other words, in silico.

#### 2.1.5. Molecular Structure and Property

After we get solution of (2.7), the nuclear repulsion

$$V_{NN}(\underline{\vec{R}}) = \frac{e^2}{4\pi\varepsilon_0} \sum_{\alpha=1}^N \sum_{\beta>\alpha}^N \frac{Z_\alpha Z_\beta}{|\vec{R}_\alpha - \vec{R}_\beta|} \quad (2.24)$$

is simply constant so can be easily calculated. Therefore, due to (2.5), (2.4) becomes the equation for nuclei.

$$\left( -\frac{\hbar^2}{2} \sum_{\alpha=1}^N \frac{1}{M_\alpha} \nabla_\alpha^2 + V_{NN}(\underline{\vec{R}}) + E_i(\underline{\vec{R}}) \right) \theta_i(\underline{\vec{R}}, t) = i\hbar \frac{\partial}{\partial t} \theta_k(\underline{\vec{R}}, t) \quad (2.25)$$

By this nuclear Hamiltonian, we can get information about energy and motion of nuclei. With minimizing the energy, optimized geometry is

<sup>②</sup> From Latin, ab initio means ‘from the beginning’ or ‘from first principles’.

<sup>③</sup> Due to the approximative  $E_{XC}$  term, sometimes including DFT into the ab initio method becomes a highly controversial topic. However, building its methodology follows the first principle so we can include DFT into the ab initio method.

obtained.

From the Hessian of energy with respect to  $\vec{R}$ , vibration of the molecule can be investigated. Likewise, computational method can be adopted to predict molecular property, for example, not only energy, structure, and vibration, but also IR, Raman, charge, MO, NMR, etc.

## 2.2. Graphene

### 2.2.1. Characteristics and Applications of Graphene

Graphene, a kind of an allotrope of carbon like  $C_{60}$ ,<sup>④</sup> diamond, and graphite, is a 2D monolayer composed of  $sp^2$  C with infinitely successive  $120^\circ$  hexagonal benzene-like rings. It has a zero-gap band structure,<sup>5</sup>  $15,000\text{ cm}^2/\text{V}\cdot\text{s}$  electron mobility at room temperature,<sup>3</sup> high opacity,<sup>5</sup>  $5,300\text{ W/m}\cdot\text{K}$  thermal conductivity,<sup>5</sup> great mechanical strength,<sup>6</sup> and  $2,630\text{ m}^2/\text{g}$  theoretical specific surface area.<sup>7</sup> Owing to such interesting properties, it has gotten enormous attention from scientists for the various application.

For example, graphene has been attempted to use for electronic, photonic, and material purpose with its novel property. In more detail, an impurity atom manipulation on graphene by electron beam,<sup>4</sup> interaction between external light and band gap of graphene,<sup>5</sup> and graphene-like  $C_2N-h2D$  structure and its characteristic properties<sup>22</sup> are noteworthy.

For chemical applications, it was studied for 2D catalytic material as well as gas sensors, for instance, oxygen reduction reaction (ORR)<sup>23</sup> and  $\text{CO}_2$  detection.<sup>24</sup> Like this, its surface interaction with small molecular entities<sup>25, 26</sup> has been utilized to application for gas storage including  $\text{CH}_4$ <sup>27</sup> and  $\text{He}$ ,<sup>28, 29</sup> and energy storage device especially for  $\text{H}_2$  storage<sup>8, 11-13</sup> and Li storage.<sup>7-10</sup>

Along the same line as the research, Li has been involved in many applications<sup>30</sup> such as graphene electrode of Li-air battery<sup>14, 15</sup> using  $\text{O}_2$ <sup>16, 18</sup> or  $\text{N}_2$ <sup>17</sup> as working material. Since the Li-air battery has very high theoretical energy density, it has been highlighted for alternative

---

<sup>④</sup> Also known as fullerene.

device of Li ion battery and power source of automotive.<sup>14</sup>

### 2.2.2. Computational Research on Graphene

Among these study on graphene, computational method has been widely adopted with DFT.<sup>6, 7, 9, 12, 13, 18, 23, 25–30</sup> The surface reactions of graphene with small chemical particles were explored.<sup>31–33</sup> Furthermore, reactivity of its various functional groups on the surface or edge was also evaluated.<sup>34</sup> Its defects<sup>35</sup> and doping by metal element<sup>36</sup> were reproduced by theoretical calculations. To improve the property of graphene, many kinds of graphene-like materials,<sup>37</sup> like graphene oxide (GO),<sup>6, 30</sup> reduced GO (rGO),<sup>6</sup> phosphorene,<sup>38</sup> and some not-yet-synthesized purely theoretical 2D lattice matter<sup>39</sup> also have been investigated.

Such computational studies on graphene have been reached for the application for energy device. For instance, graphene–lithium system has attracted recent interest in rechargeable battery,<sup>7, 9</sup> H<sub>2</sub> storage material,<sup>12, 13</sup> and electrode of Li–air battery.<sup>18</sup>

In terms of Li–air battery, the main interest of study was lithium–oxygen system. Previous research focused on O<sub>2</sub>, LiO<sub>2</sub>, and Li<sub>2</sub>O<sub>2</sub> rather than various molecules in ambient air.<sup>14–16, 18, 40</sup> To achieve practical application of Li–air battery, further studies on the interaction between graphene–lithium system and air molecule are still required.<sup>15</sup> In addition, such evaluations under ambient condition will be helpful to acquire useful insight for other practical application, like H<sub>2</sub> storage.

## Chapter 3. Computational Details

### 3.1. Simulations of Binding Mechanism of Air Molecules to Graphene–Lithium System

In this study, graphene nanoflake (GR) was introduced to represent real graphene. Below is the procedure of preparation of graphene–lithium system in detail.

- a. The GR composed of 37 hexagonal rings, GR(37), was fully optimized.
- b. Li or  $\text{Li}^+$  was located on a central ring of the optimized GR(37), and fully optimized to build  $\text{GR}(37)-\text{Li}/\text{Li}^+$ .
- c. The fully optimized structure of  $\text{GR}(37)-\text{M}$  ( $\text{M} = \text{Li}, \text{Li}^+$ ) was compared with previous study,<sup>12</sup> to test the reproducibility of computation.

To the  $\text{GR}(37)-\text{M}$ , binding of  $\text{N}_2$ ,  $\text{O}_2$ , or Ar was simulated. Since bimolecular collision is predominant over termolecular collision in room temperature and pressure,<sup>41</sup> all the binding mechanisms were presumed stepwise mechanism, not concerted. Below is the procedure in detail.

- a. One of  $\text{N}_2$ ,  $\text{O}_2$ , or Ar was located at short distance from  $\text{Li}/\text{Li}^+$  and fully optimized to build  $\text{GR}(37)-\text{M}-\text{A}$  ( $\text{A} = \text{N}_2, \text{O}_2, \text{Ar}$ ).
- b. The fully optimized structure of  $\text{GR}(37)-\text{M}-\text{A}$  was followed by frequency calculation. If any imaginary frequency had been found, an attempt to remove the imaginary frequency was proceeded, to get real minimum structure.
- c. After the real minimum structure of  $\text{GR}(37)-\text{M}-\text{A}$  was verified, second A was introduced to the structure. Optimization and frequency calculation were performed again to get structure of  $\text{GR}(37)-\text{M}-\text{A}_2$ .
- d. The procedure a.–c. was iteratively repeated to get the third, the fourth, and all  $n$ th structure of  $\text{GR}(37)-\text{M}-\text{A}_n$  where  $n$  is

the number of binding A, until any inexpungible instability was discovered.

### 3.2. Quantitative Details of the Method

All computations employed DFT and were performed by Gaussian 16.<sup>42</sup> UCAM–B3LYP functional<sup>43</sup> and 6–311G(d,p) basis set<sup>44</sup> were adopted. Using the results, the obtained structures were analyzed.

The binding energy was calculated in terms of average<sup>12, 29</sup> and step:<sup>29</sup>

$$E_{bind,avg}(n, A) = \frac{E(\text{GR}(37) - M - A_n) - E(\text{GR}(37) - M) - nE(A)}{n} \quad (3.1)$$

and

$$E_{bind,step}(n, A) = E(\text{GR}(37) - M - A_n) - E(\text{GR}(37) - M - A_{n-1}) - E(A) \quad (3.2)$$

respectively, where  $E_{bind,avg}(n, A)$  is the average binding energy of  $n$  A,  $E_{bind,step}(n, A)$  is the stepwise binding energy of  $n$ th A, and  $E(X)$  is the total energy of X. If  $E_{bind,avg}(n, A)$  or  $E_{bind,step}(n, A)$  is negative, the formation of the binding structure will be exothermic.

For further analysis, the atomic charge values were obtained by natural population analysis (NPA) method.<sup>45</sup>

The same level of theory was successfully applied to many previous studies within graphene and small molecular entities.<sup>9, 12, 13, 31, 32</sup> Thus, it was adopted in this study again for reliability and convenient comparison. However, due to the more electrons of Ar, N<sub>2</sub>, and O<sub>2</sub> than H<sub>2</sub>, the D3<sup>46</sup> and D3(BJ)<sup>47</sup> dispersion corrections were tested. In more detail, several structures from UCAM–B3LYP/6–311G(d,p) were reoptimized by D3 and D3(BJ) and the resultant geometry, energy, and NPA charge were analyzed.

### 3.3. Effects of Several Relevant Factors to the Binding

## Mechanism

To thoroughly understand the GR(37)–M–A<sub>n</sub> system, some additional analyses were performed as below.

- a. The effect of Li species was investigated. The binding structure of an air molecule onto pristine GR(37), GR(37)–A, was simulated for comparison.
- b. Both singlet and triplet spin states of O<sub>2</sub> were investigated. Under these two spin states, GR(37)–Li/Li<sup>+</sup>–O<sub>2</sub> were simulated for comparison.
- c. The effect of GR(37) was investigated. From fully optimized GR(37)–M–A<sub>n</sub>, GR(37) was removed to build M–A<sub>n</sub> and its energy parameters were calculated.

# Chapter 4. Results

## 4.1. Reproducibility

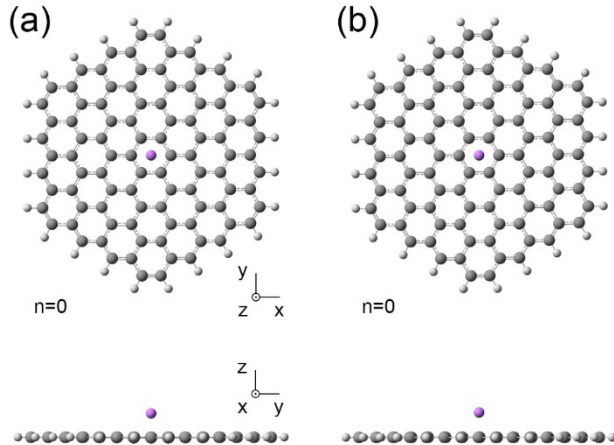


**Figure 1.** Top and side view of fully optimized structures of (a) GR(37)-Li, and (b) GR(37)-Li<sup>+</sup>. All computational works were performed by UCAM-B3LYP/6-311G(d,p) level.

**Table 1.** Height of Li/Li<sup>+</sup> from GR(37) (Å) Calculated at the UCAM-B3LYP/6-311G(d,p) Level

Origin	GR(37)-Li	GR(37)-Li <sup>+</sup>
Previous Report <sup>12</sup>	1.735	1.771
In This Work	1.736	1.771

Figure 1 shows the fully optimized structures of GR(37)-Li/Li<sup>+</sup>. The height of Li/Li<sup>+</sup> from GR(37),  $h$ , is listed in Table 1, with previously reported values. The  $h$  values from this work were well agreed with previous report. Because structure is a foundation of property in computational chemistry,<sup>2</sup> reproducibility of calculations in this work was verified by the agreement.

## 4.2. Effects of Li/Li<sup>+</sup> to the Binding Mechanism

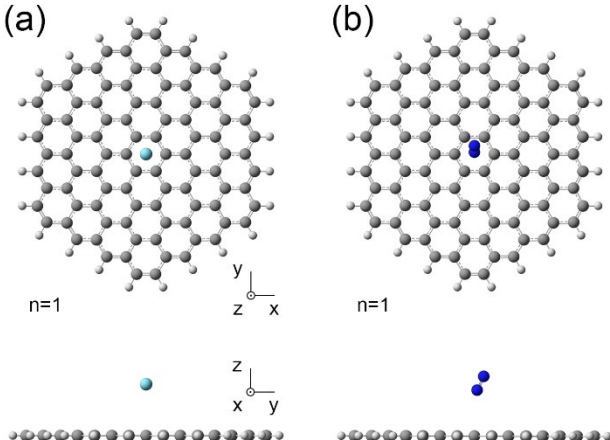


**Figure 2.** Top and side view of fully optimized structures of (a) GR(37)–Ar, and (b) GR(37)–N<sub>2</sub>. Structure of GR(37)–O<sub>2</sub> was never obtained. All computational works were performed by UCAM–B3LYP/6–311G(d,p) level.

Figure 2 shows the fully optimized structures of GR(37)–Ar/N<sub>2</sub>. The height of Ar and N<sub>2</sub> were 3.680 Å and 3.293 Å, respectively. Structure of GR(37)–O<sub>2</sub> was never obtained due to the divergence with O<sub>2</sub> moving apart from GR(37).

Figure 4(a), 8(a), and 12(a) show structures of GR(37)–Li with one Ar, N<sub>2</sub>, and O<sub>2</sub>, respectively.  $R(M – A)$ , distance between M and A, were  $R(Li – Ar) = 2.455$  Å,  $R(Li – N) = 2.086$  Å for closer N, and  $R(Li – O) = 2.042$  Å for closer O. In addition, Figure 6(a), 10(a), and 14(a) show structures of GR(37)–Li<sup>+</sup> with one Ar, N<sub>2</sub>, and O<sub>2</sub>, respectively, and these positively charged structures were similar to the neutral structures.

These results clearly show the role of Li/Li<sup>+</sup>. They shortened the binding distance, so the binding of an air molecule onto GR(37) was enhanced. Furthermore, the unobtainable binding of O<sub>2</sub> was achieved by Li/Li<sup>+</sup>. Therefore, it is sure that Li/Li<sup>+</sup> greatly assist the binding of an air molecule onto GR(37). This is in accord with previous experimental results that some kinds of vapor molecules are adsorbed on graphene much better before cleaning step than after cleaning step.<sup>48</sup>

In this calculation, all O<sub>2</sub> molecules of the calculations were considered as spin triplet state.

#### 4.3. Effects of Spin State of O<sub>2</sub> to Binding Mechanism

Structure of GR(37)–Li–O<sub>2</sub> with the singlet O<sub>2</sub> was never obtained due to the divergence with Li–O<sub>2</sub> complex moving away from center to edge, whereas the structure from the triplet O<sub>2</sub> is shown in Figure 12(a). It was obvious that O<sub>2</sub> maintains its triplet state during binding onto GR(37)–Li.

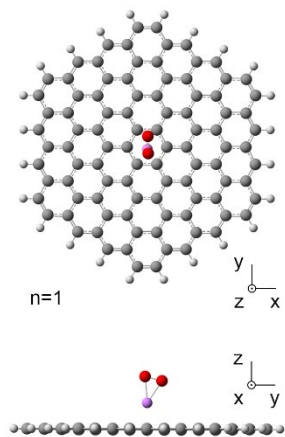


**Figure 3.** Top and side view of fully optimized structures of GR(37)–Li<sup>+</sup>–O<sub>2</sub> from the singlet O<sub>2</sub>. The computational work was performed by UCAM–B3LYP/6–311G(d,p) level.

Structure of GR(37)–Li<sup>+</sup>–O<sub>2</sub> with the singlet and the triplet O<sub>2</sub> is shown in Figure 3 and 14(a), respectively. The structure in Figure 3 resembled lithium superoxide LiO<sub>2</sub>,<sup>49</sup> although the structure in Figure 14(a) was analogous to biochemical O<sub>2</sub>–metal–binding system.<sup>50</sup> In addition, since triplet O<sub>2</sub> structure had 128 kJ/mol lower energy, it would be obvious that GR(37)–Li<sup>+</sup>–O<sub>2</sub> possesses the triplet O<sub>2</sub>.

Thus, it is sure that O<sub>2</sub> molecule keeps its triplet state when it is bound to GR(37)–Li/Li<sup>+</sup>, and changes to singlet state to construct LiO<sub>2</sub>. This is in accord with previous experimental result that LiO<sub>2</sub> has singlet O<sub>2</sub>.<sup>49</sup> Thus, the structure from singlet O<sub>2</sub> is LiO<sub>2</sub> rather

than O<sub>2</sub> molecule, so all O<sub>2</sub> molecules in this work were considered as triplet state.

#### 4.4. Binding Structures of Ar/N<sub>2</sub>/O<sub>2</sub> to GR(37)–Li/Li<sup>+</sup>

##### 4.4.1. Ar on GR(37)–Li/Li<sup>+</sup>

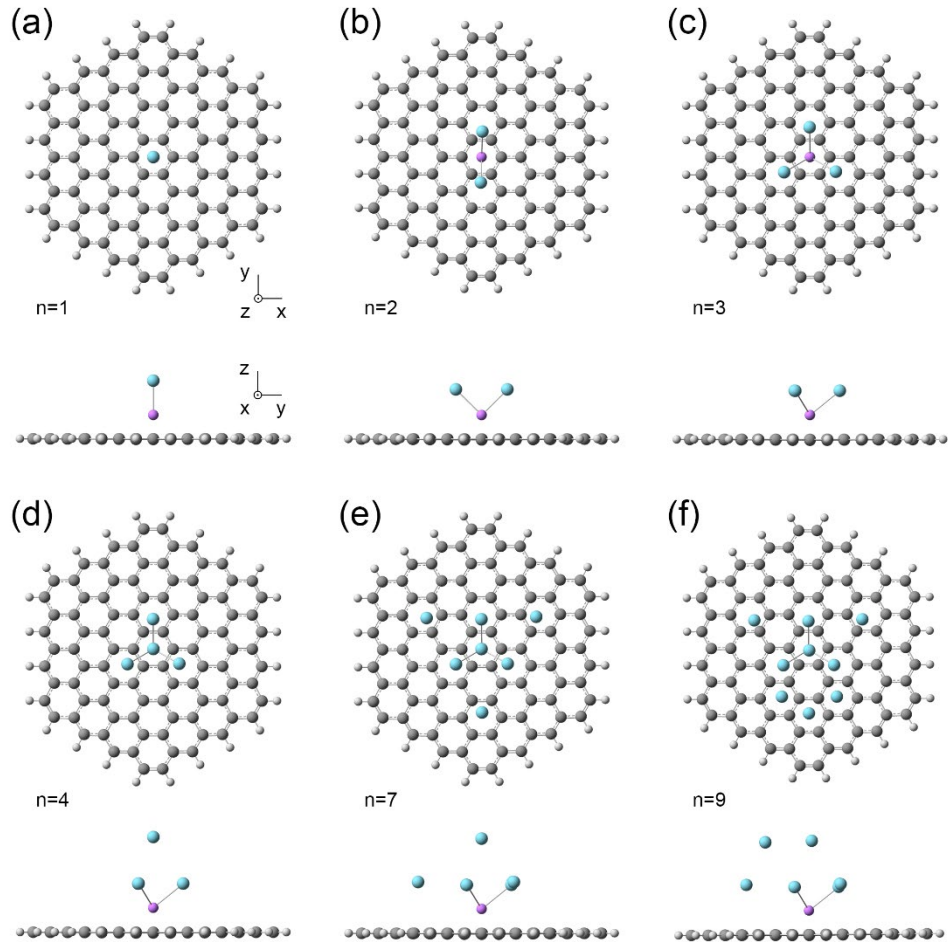


**Figure 4.** Top and side view of fully optimized structures of GR(37)–Li–Ar<sub>n</sub> for (a)  $n = 1$ , (b)  $n = 2$ , (c)  $n = 3$ , (d)  $n = 4$ , (e)  $n = 7$ , and (f)  $n = 9$ . All computational works were performed by UCAM–B3LYP/6–311G(d,p) level.

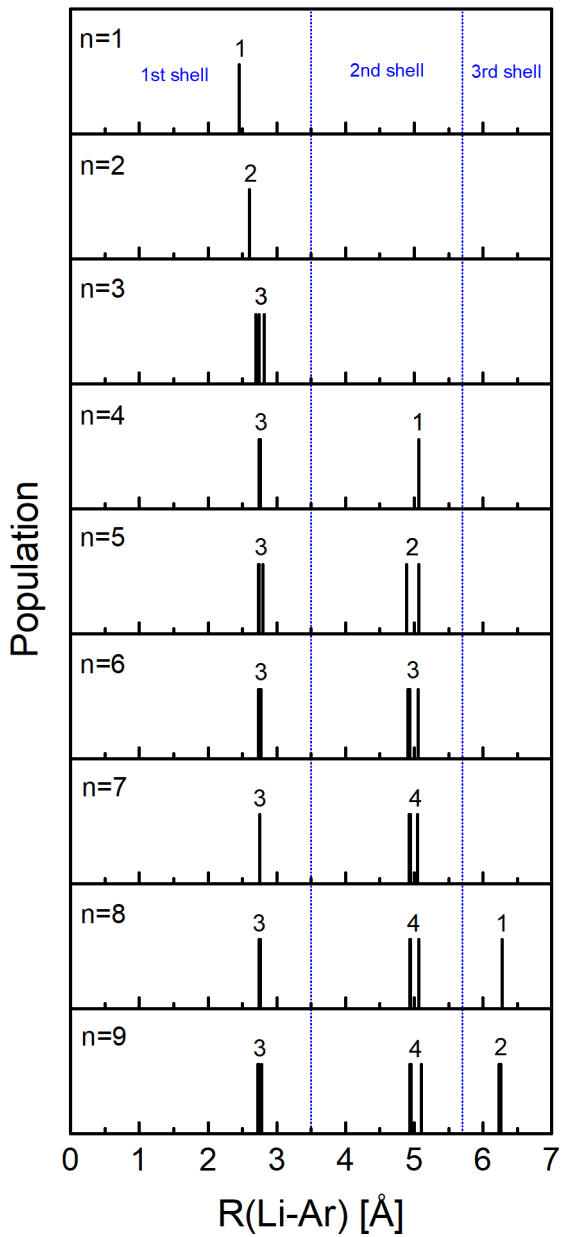


**Figure 5.** Stick diagrams of  $R(\text{Li}-\text{Ar})$  from GR(37)- $\text{Li}-\text{Ar}_n$ . Above the sticks, the degeneracy of binding is denoted. All computational works were performed by UCAM-B3LYP/6-311G(d,p) level.

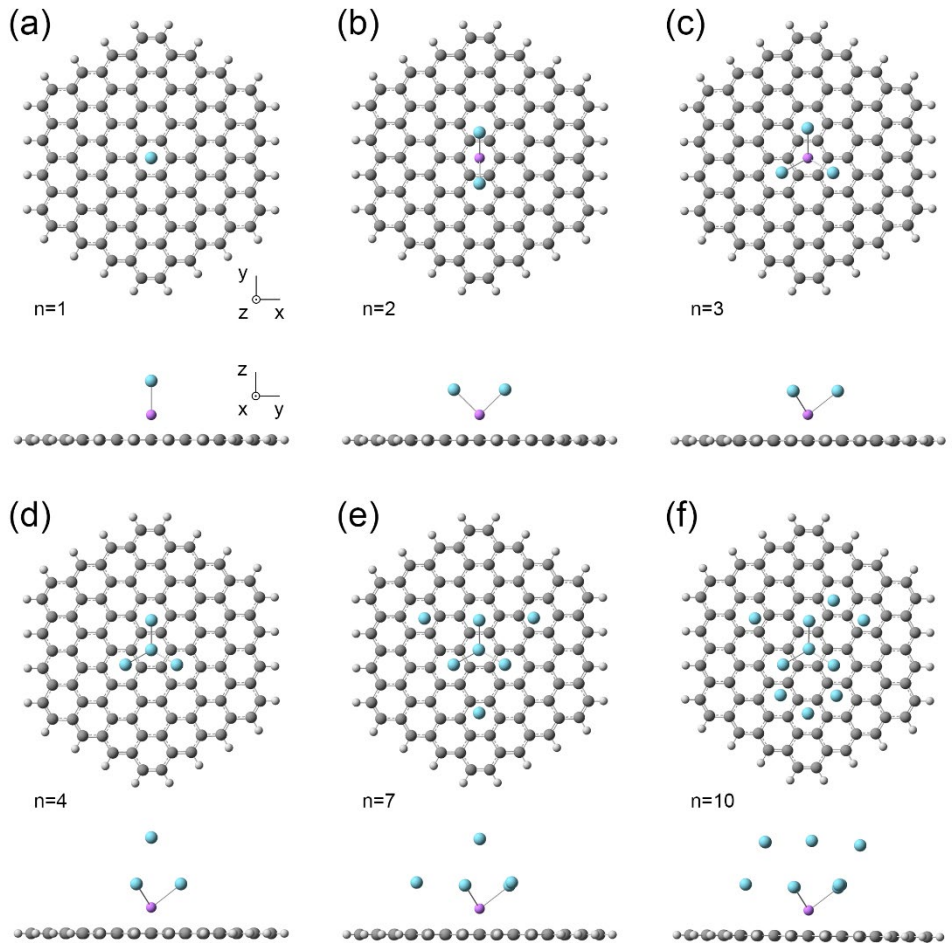


**Figure 6.** Top and side view of fully optimized structures of GR(37) $-$  $\text{Li}^+$  $-$  $\text{Ar}_n$  for (a)  $n = 1$ , (b)  $n = 2$ , (c)  $n = 3$ , (d)  $n = 4$ , (e)  $n = 7$ , and (f)  $n = 10$ . All computational works were performed by UCAM-B3LYP/6–311G(d,p) level.

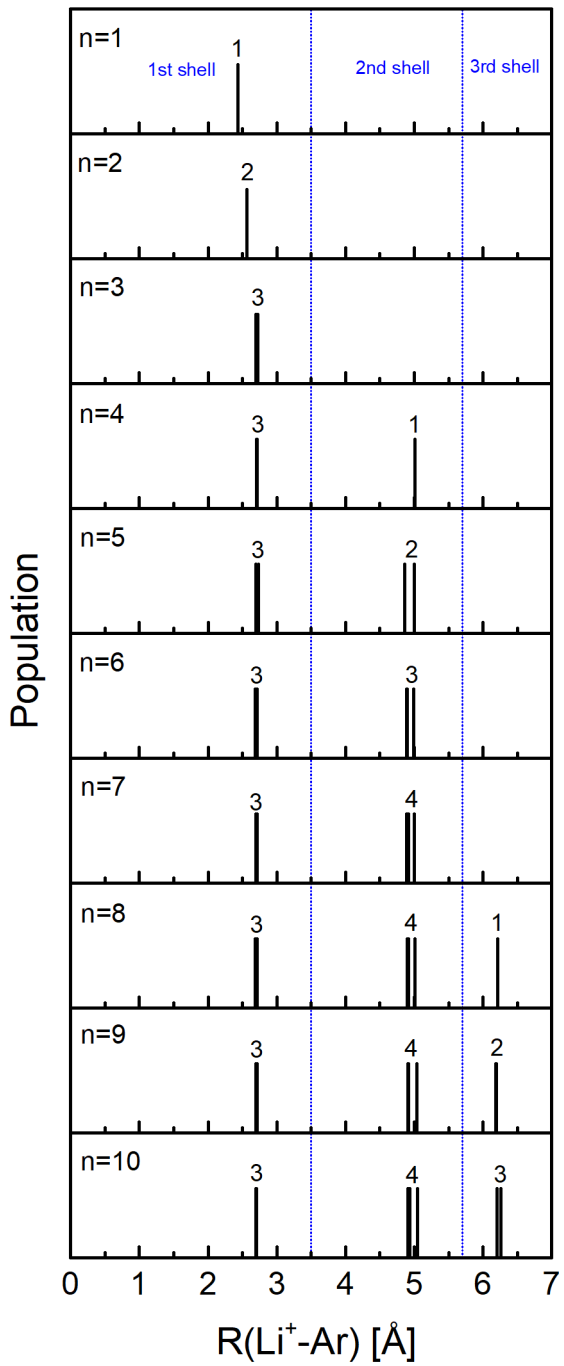


**Figure 7.** Stick diagrams of  $R(\text{Li}^+ - \text{Ar})$  from GR(37)- $\text{Li}^+ - \text{Ar}_n$ . Above the sticks, the degeneracy of binding is denoted. All computational works were performed by UCAM-B3LYP/6-311G(d,p) level.

Figure 4 shows the fully optimized structures of GR(37)–Li–Ar<sub>*n*</sub> for *n* = 1, 2, 3, 4, 7, and 9, and Figure 5 shows the stick diagrams of *R*(Li–Ar) from the GR(37)–Li–Ar<sub>*n*</sub> for *n* = 1–9.

For *n* = 1, the Ar molecule was perpendicular to GR(37), and *R*(Li–Ar) = 2.455 Å. For *n* = 2, the Ar molecules at 180° were between C atoms from top view, and *R*(Li–Ar) = 2.598 and 2.598 Å. For *n* = 3, the Ar molecules at 120° avoided to be directly on C atoms from top view again, and *R*(Li–Ar) = 2.692, 2.746, and 2.817 Å. The Ar molecules were located to minimize repulsion from each other and C of GR(37). Since the addition of Ar molecule slightly elongated the *R*(Li–Ar), it would be sure that the first three Ar molecules interact each other.

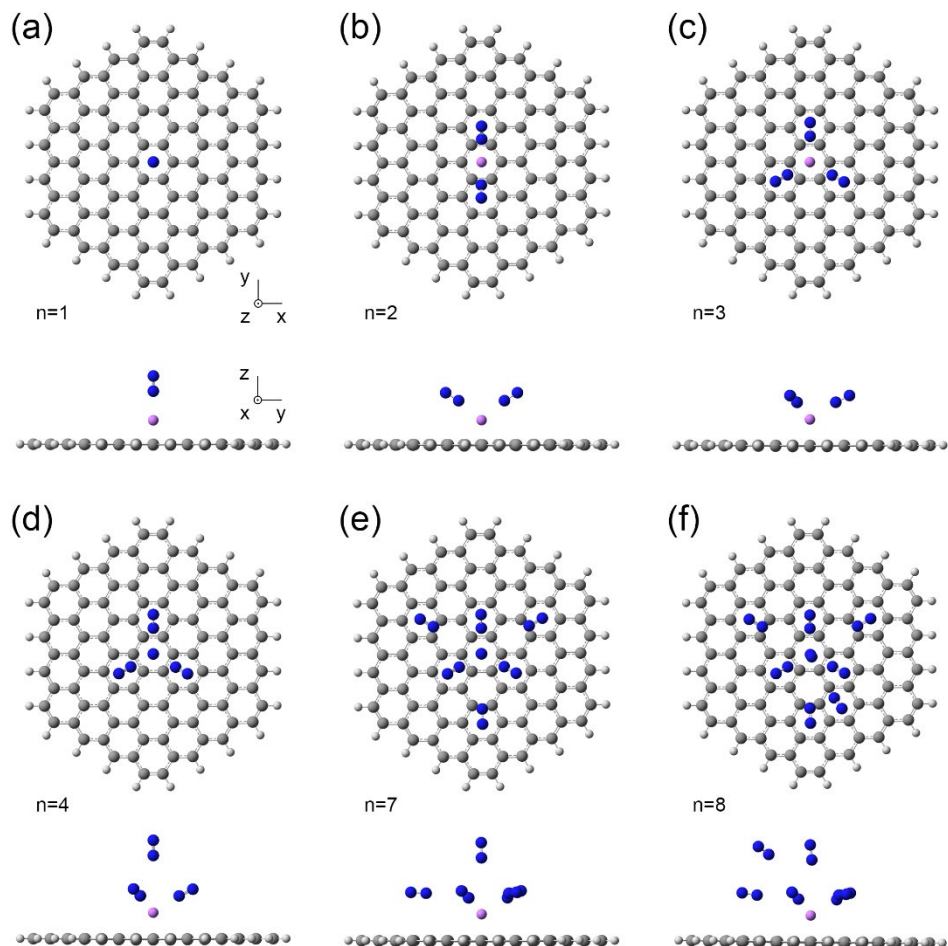
For *n* = 4, *R*(Li–Ar) = 2.745, 2.755, 2.760, and 5.069 Å. The three Ar molecules almost maintained their *R*(Li–Ar), but the fourth *R*(Li–Ar) significantly lengthened. Further addition of Ar molecule showed the same aspect. From these tendencies, the interactive direct binding of three molecules and indirect binding of the additional molecules were revealed.

The evolution of the GR(37)–Li–Ar<sub>*n*</sub> structures discovered shell structures. The first shell was composed of three direct interacting Ar molecules, and the additional four molecules were placed in the second shell. The third shell was confirmed by the eighth and the ninth molecule. These structures were analogous to the solvation shell structure.<sup>51</sup>

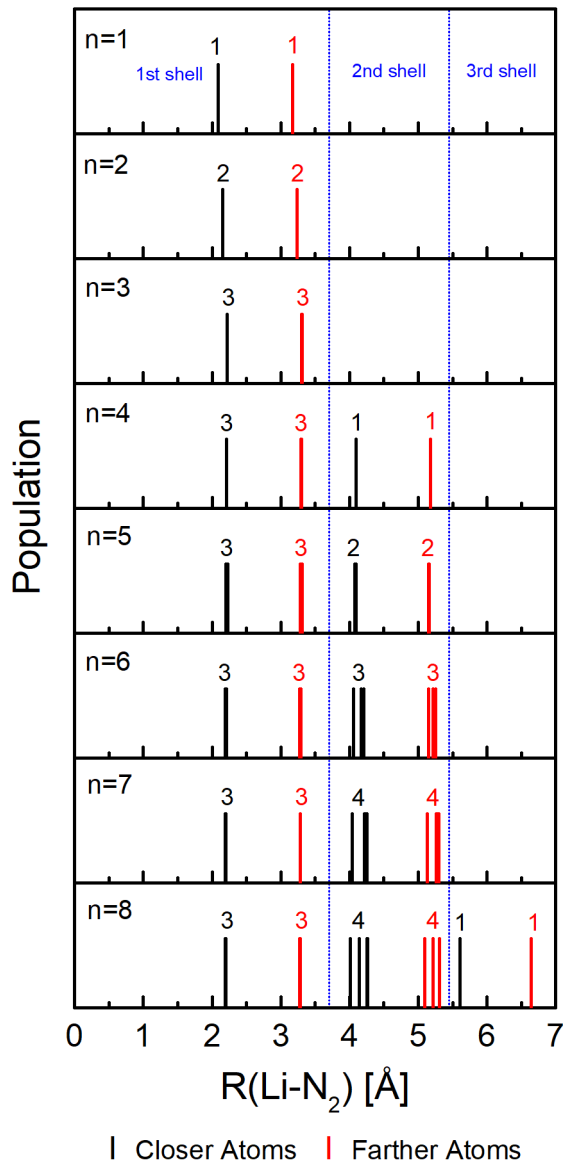
Due to the repulsion from symmetric C of GR(37), GR(37)–Li–Ar<sub>3</sub> possesses high symmetry. From the direct binding structure, the additional indirectly bound molecules also were placed to symmetric position. In turn, symmetric surface structure induced symmetric cluster structure.

Figure 6 shows the fully optimized structures of GR(37)–Li<sup>+</sup>–Ar<sub>*n*</sub> for *n* = 1, 2, 3, 4, 7, and 10, and Figure 7 shows the stick diagrams of *R*(Li<sup>+</sup>–Ar) from the GR(37)–Li<sup>+</sup>–Ar<sub>*n*</sub> for *n* = 1–10. The results from charged structures were similar to the results from neutral structures.

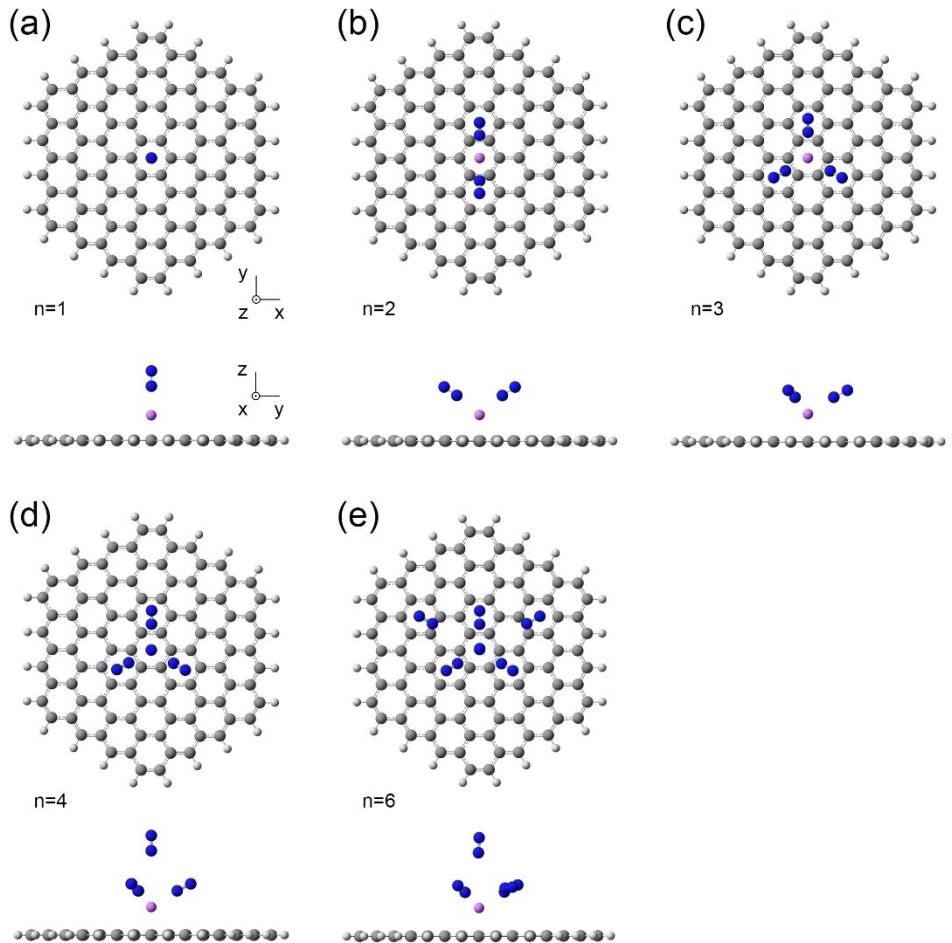
#### 4.4.2. N<sub>2</sub> on GR(37)–Li/Li<sup>+</sup>



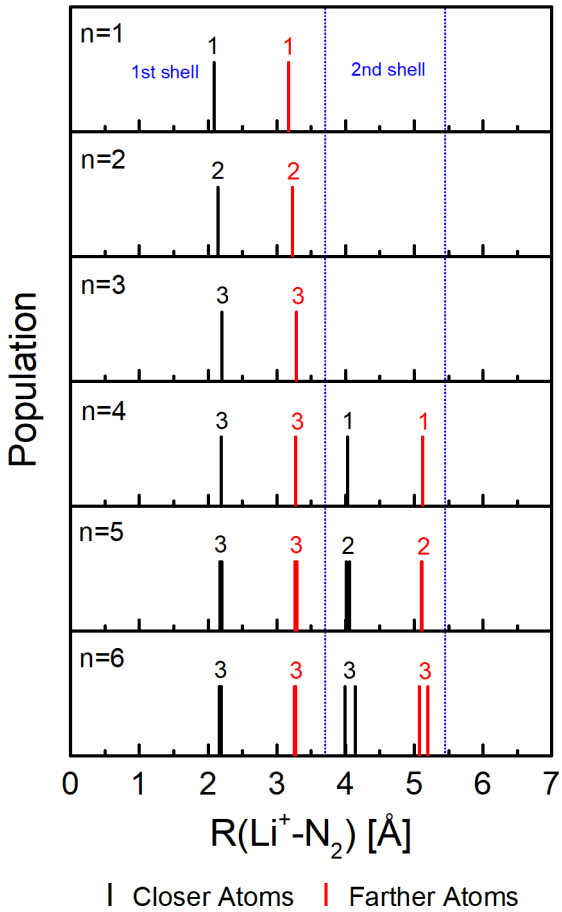
**Figure 8.** Top and side view of fully optimized structures of GR(37)–Li–(N<sub>2</sub>)<sub>n</sub> for (a)  $n = 1$ , (b)  $n = 2$ , (c)  $n = 3$ , (d)  $n = 4$ , (e)  $n = 7$ , and (f)  $n = 8$ . All computational works were performed by UCAM–B3LYP/6–311G(d,p) level.



**Figure 9.** Stick diagrams of  $R(\text{Li} - \text{N}_2)$  from GR(37)-Li-( $\text{N}_2$ ) $_n$ . Above the sticks, the degeneracy of binding is denoted. All computational works were performed by UCAM-B3LYP/6-311G(d,p) level.



**Figure 10.** Top and side view of fully optimized structures of  $\text{GR}(37)-\text{Li}^+-(\text{N}_2)_n$  for (a)  $n = 1$ , (b)  $n = 2$ , (c)  $n = 3$ , (d)  $n = 4$ , and (e)  $n = 6$ . (e)  $\text{GR}(37)-\text{Li}^+-(\text{N}_2)_6$  has an imaginary frequency with twisting motion of hexagonal rings of  $\text{GR}(37)$  at  $-910.82 \text{ cm}^{-1}$ . All computational works were performed by UCAM-B3LYP/6-311G(d,p) level.



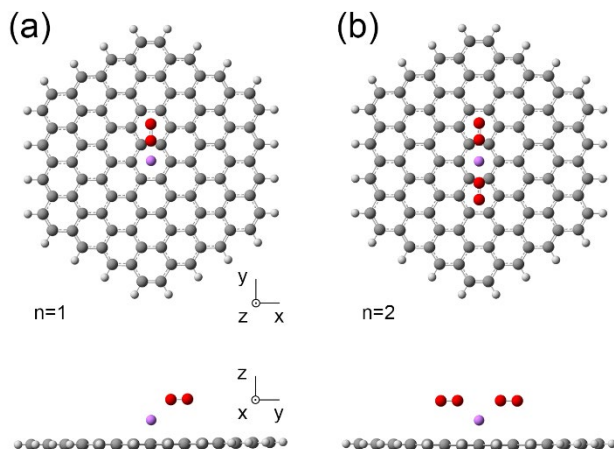
**Figure 11.** Stick diagrams of  $R(\text{Li}^+ - \text{N}_2)$  from GR(37)-Li<sup>+</sup>-(N<sub>2</sub>)<sub>n</sub>. Above the sticks, the degeneracy of binding is denoted. All computational works were performed by UCAM-B3LYP/6-311G(d,p) level.

Figure 8 shows the fully optimized structures of GR(37)-Li-(N<sub>2</sub>)<sub>n</sub> for  $n = 1, 2, 3, 4, 7$ , and 8, and Figure 9 shows the stick diagrams of  $R(\text{Li} - \text{N}_2)$  from the GR(37)-Li-(N<sub>2</sub>)<sub>n</sub> for  $n = 1-8$ . Figure 10 shows the fully optimized structures of GR(37)-Li<sup>+</sup>-(N<sub>2</sub>)<sub>n</sub> for  $n = 1, 2, 3, 4$ , and 6, and Figure 11 shows the stick diagrams of  $R(\text{Li}^+ - \text{N}_2)$  from the GR(37)-Li<sup>+</sup>-(N<sub>2</sub>)<sub>n</sub> for  $n = 1-6$ . The results from charged structures were similar to the results from neutral structures.

Overall trend was analogous to the clusters of Ar, but unlike monatomic Ar, diatomic N<sub>2</sub> showed orientational effects. The

innermost three N<sub>2</sub> molecules were directly bound with linear end-on structures, like previous experimental report about coordination compound of N<sub>2</sub> ligand.<sup>52</sup> Because of such linear structures, the additional N<sub>2</sub> molecules were radially stacked to maximize contact area. Thus, end-on structures were indirectly repeated, and the symmetry was preserved.

#### 4.4.3. O<sub>2</sub> on GR(37)–Li/Li<sup>+</sup>



**Figure 12.** Top and side view of fully optimized structures of GR(37)–Li–(O<sub>2</sub>)<sub>n</sub> for (a)  $n = 1$ , and (b)  $n = 2$ . (b) GR(37)–Li–(O<sub>2</sub>)<sub>2</sub> has an imaginary frequency with flapping motion of +y and -y parts of GR(37) to +z and -z direction simultaneously at  $-1.53\text{ cm}^{-1}$ . All computational works were performed by UCAM–B3LYP/6–311G(d,p) level.

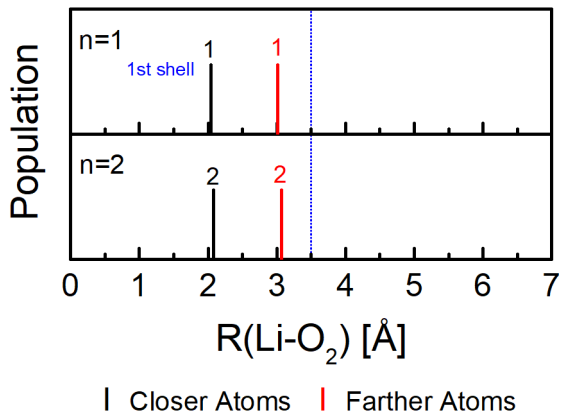


**Figure 13.** Stick diagrams of  $R(\text{Li}-\text{O}_2)$  from GR(37)-Li- $(\text{O}_2)_n$ . Above the sticks, the degeneracy of binding is denoted. All computational works were performed by UCAM-B3LYP/6-311G(d,p) level.

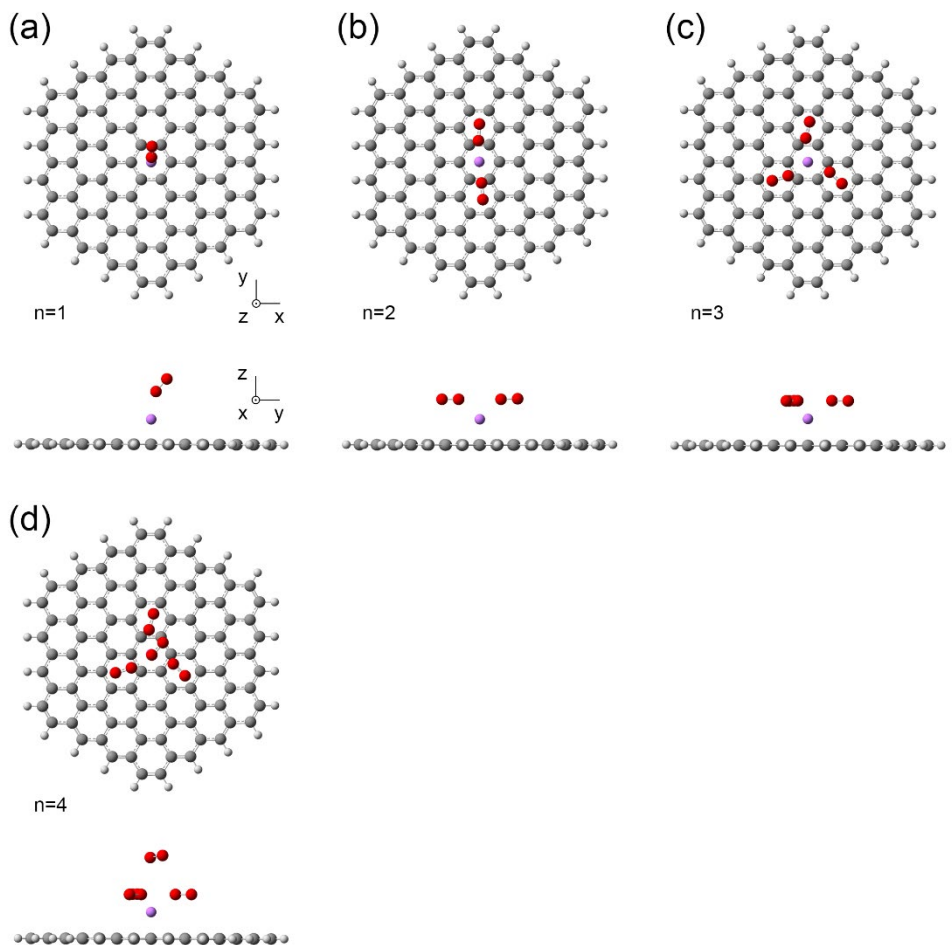


**Figure 14.** Top and side view of fully optimized structures of GR(37) $\text{--Li}^{\text{+}}\text{--}(\text{O}_2)_n$  for (a)  $n = 1$ , (b)  $n = 2$ , (c)  $n = 3$ , and (d)  $n = 4$ . All computational works were performed by UCAM–B3LYP/6–311G(d,p) level.

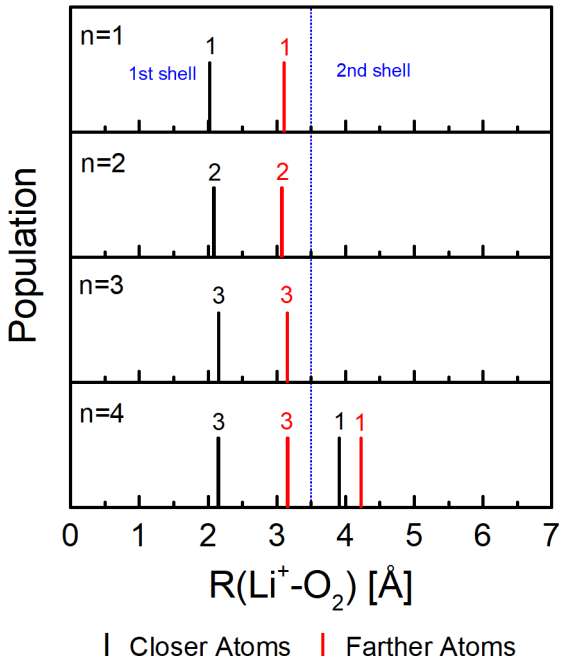


**Figure 15.** Stick diagrams of  $R(\text{Li}^+ - \text{O}_2)$  from  $\text{GR}(37)-\text{Li}^+-(\text{O}_2)_n$ . Above the sticks, the degeneracy of binding is denoted. All computational works were performed by UCAM-B3LYP/6-311G(d,p) level.

Figure 12 shows the fully optimized structures of  $\text{GR}(37)-\text{Li}-(\text{O}_2)_n$  for  $n = 1$ , and 2, and Figure 13 shows the stick diagrams of  $R(\text{Li} - \text{O}_2)$  from the  $\text{GR}(37)-\text{Li}-(\text{O}_2)_n$  for  $n = 1$ , and 2. Figure 14 shows the fully optimized structures of  $\text{GR}(37)-\text{Li}^+-(\text{O}_2)_n$  for  $n = 1, 2, 3$ , and 4, and Figure 15 shows the stick diagrams of  $R(\text{Li}^+ - \text{O}_2)$  from the  $\text{GR}(37)-\text{Li}^+-(\text{O}_2)_n$  for  $n = 1-4$ . The results from charged structures were similar to the results from neutral structures.

Overall trend was analogous to the clusters of Ar, except confirmation of the third shell.  $\text{O}_2$  also showed orientational effects, but unlike  $\text{N}_2$ , the innermost three  $\text{O}_2$  molecules were bound with bent end-on structures, like well-known biochemical structures of hemoglobin.<sup>50</sup> Because of such bent structures, the fourth  $\text{O}_2$  was stacked with side-on structure to maximize contact area. Thus, end-on structures and the symmetry were dissipated.

#### 4.5. Charge of Li/Li<sup>+</sup> and GR(37)

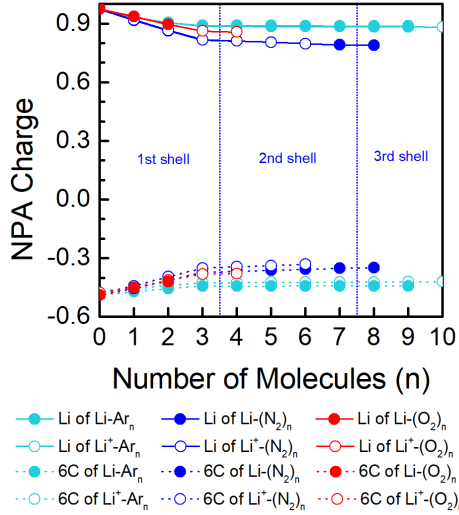


**Figure 16.** NPA Charge of the Li/Li<sup>+</sup> and the central ring of GR(37). All computational works were performed by UCAM–B3LYP/6–311G(d,p) level.

Figure 16 shows the NPA charge of the Li/Li<sup>+</sup> and the central ring of GR(37). For  $n = 0$ , Li and Li<sup>+</sup> had 0.973 and 0.976 charge, respectively. The charges clearly decreased until  $n = 3$ , and relatively gradually decreased for  $n = 3–10$ . It resulted from the direct interaction of the molecules in the first shell and the indirect binding of the additional molecules.

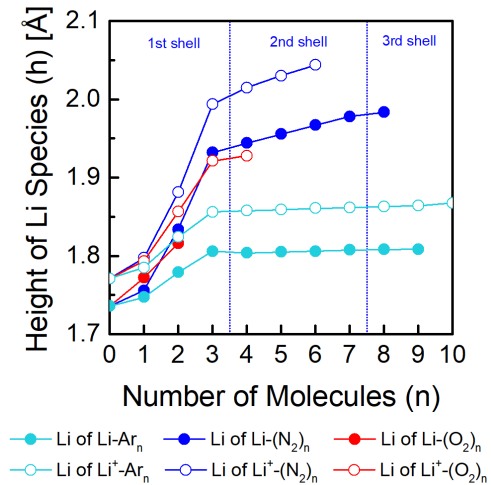
The N<sub>2</sub> showed the fastest decreasing trend of the charge of Li/Li<sup>+</sup>, followed by O<sub>2</sub>, and Ar. It is evidence of the strongest electron donating ability of N<sub>2</sub> for coordination, followed by O<sub>2</sub>, and Ar.

In addition, plots of Li and Li<sup>+</sup> distinctly overlapped each other. In other words, no matter what initial charge of the Li species was, Li/Li<sup>+</sup> finally had almost same charges.

The plots of the central ring were almost upside-down inversion of the plots of Li/Li<sup>+</sup>, with –0.489 and –0.477 charge of the central ring of GR(37)–Li and GR(37)–Li<sup>+</sup> for  $n = 0$ , respectively. Unlike

$\text{Li}/\text{Li}^+$ , the plots of positive systems were above the corresponding plots of neutral system. It is evidence of dispersion of positive charge onto GR(37), rather than confinement in  $\text{Li}^+$ .

#### 4.6. Height of $\text{Li}/\text{Li}^+$ from GR(37)



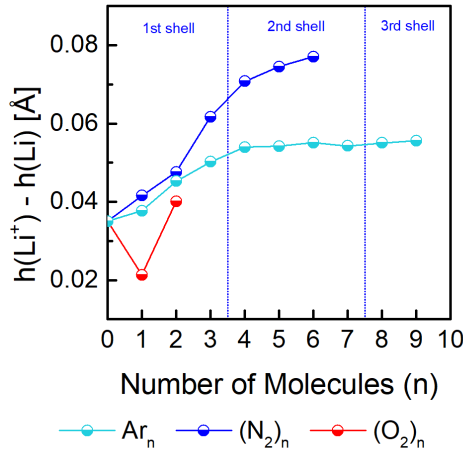
**Figure 17.** Height of the  $\text{Li}/\text{Li}^+$  from the GR(37). All computational works were performed by UCAM–B3LYP/6–311G(d,p) level.

Figure 17 shows the height of the  $\text{Li}/\text{Li}^+$  from the GR(37),  $h$ , and last row of Table 1 shows the  $h$  for  $n = 0$ . Aspects of  $h$  can be explained by the charge distribution.

##### 4.6.1. Analysis with Local Charge of the Central Ring

As shown in Figure 16, positive charge of  $\text{Li}/\text{Li}^+$  and negative charge of the central ring quickly approached to 0 for  $n = 0–3$ , and they slowed down for  $n = 3–10$ . Thus, decreasing trend of electrostatic attraction between the  $\text{Li}/\text{Li}^+$  and the central ring was quick for  $n = 0–3$ , and slow for  $n = 3–10$ . Consequently, the  $h$  increased at a fast rate for  $n = 0–3$ , and slow rate for  $n = 3–10$ .

Because the most drastic change of charge occurred with  $\text{N}_2$ , followed by  $\text{O}_2$ , and  $\text{Ar}$ , the  $h$  with  $\text{N}_2$  ascended most rapidly, followed by  $\text{O}_2$ , and  $\text{Ar}$ .



**Figure 18.** Difference of height of  $\text{Li}/\text{Li}^+$  from GR(37). All computational works were performed by UCAM–B3LYP/6–311G(d,p) level.

Figure 18 shows height difference,  $h(\text{Li}^+) - h(\text{Li})$ , where  $h(\text{Li}^+)$  and  $h(\text{Li})$  are  $h$  of  $\text{Li}^+$  and  $\text{Li}$ , respectively. In Figure 16, the central ring charge difference between positive system and negative system was getting greater in the first shell and relatively alleviated in the additional shells, so increment of the height difference was most steep in the first shell and diminished in the additional shells.

In addition,  $\text{N}_2$  showed the greatest charge difference, followed by  $\text{Ar}$ , and  $\text{O}_2$ , so  $\text{N}_2$  resulted in the greatest  $h$  difference, followed by  $\text{Ar}$ , and  $\text{O}_2$ .

#### 4.6.2. Analysis with Total Charge of the GR(37)

Due to the law of charge conservation, it is obvious that

$$Q_{\text{Li}} + Q_{\text{GR}(37)} = 0 \quad (4.1)$$

for neutral  $\text{GR}(37)-\text{Li}-\text{A}_n$ , and

$$Q_{\text{Li}^+} + Q_{\text{GR}(37)} = 1 \quad (4.2)$$

for positive  $\text{GR}(37)-\text{Li}^+-\text{Ar}_n$ , where  $Q_{\text{Li}}$ ,  $Q_{\text{Li}^+}$ , and  $Q_{\text{GR}(37)}$  are charge of Li,  $\text{Li}^+$ , and GR(37), respectively. For instance, according to previously mentioned charge of Section 4.5. for  $n = 0$ ,  $\text{GR}(37)-\text{Li}$  had  $Q_{\text{Li}} = 0.973$  and  $Q_{\text{GR}(37)} = -0.973$ , and  $\text{GR}(37)-\text{Li}^+$  had  $Q_{\text{Li}^+} = 0.976$  and  $Q_{\text{GR}(37)} = 0.024$ , so Li and  $\text{Li}^+$  felt electrostatic attraction and repulsion, respectively. For these reasons,  $\text{Li}^+$  was higher than corresponding Li, for all  $n$ . Figure 17 and 18 clearly shows this tendency. In Figure 17, the  $h$  of  $\text{Li}^+$  was always greater than the corresponding  $h$  of Li, so all  $h(\text{Li}^+) - h(\text{Li})$  values in Figure 18 were positive.

#### 4.7. Binding Energy of Ar/N<sub>2</sub>/O<sub>2</sub> to GR(37)-Li/Li<sup>+</sup>

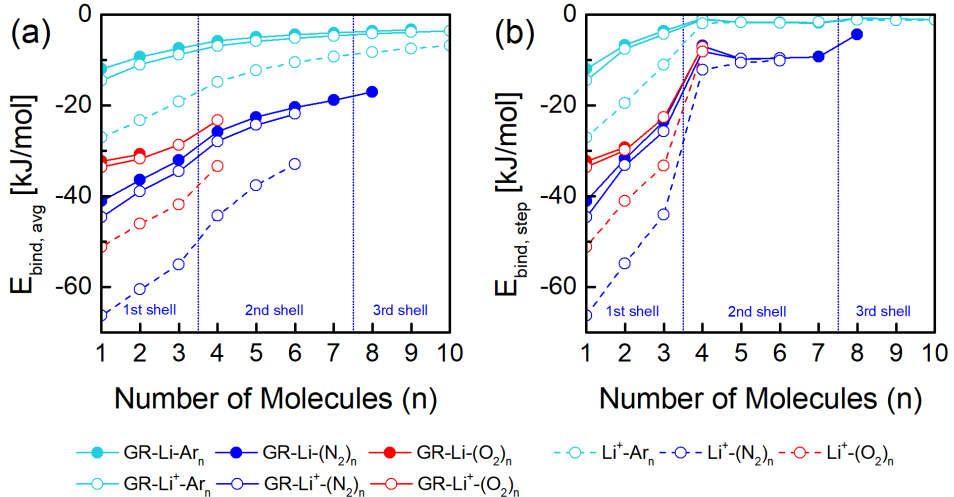


**Figure 19.** (a) Average and (b) stepwise binding energy of Ar,  $\text{N}_2$ , and  $\text{O}_2$  to  $\text{GR}(37)-\text{Li}/\text{Li}^+$  and  $\text{Li}^+$ . All computational works were performed by UCAM-B3LYP/6-311G(d,p) level.

Figure 19 shows the (a) average and (b) stepwise binding energy of Ar,  $\text{N}_2$ , and  $\text{O}_2$  molecules onto  $\text{GR}(37)-\text{Li}/\text{Li}^+$ . Both neutral and positive systems showed similar tendencies, but the binding of the positive system was slightly more exothermic.

In Figure 19(a), all average plots had converging trend. In more detail, stepwise plots in Figure 19(b) rapidly approached to 0 in the

first shell, and steadily maintained in the additional shells. These tendencies were another evidence of the direct interaction in the first shell and the indirect binding in the additional shells.

The most exothermic trend was calculated with  $\text{N}_2$ , followed by  $\text{O}_2$ , and Ar. Therefore, as shown in Section 4.5.,  $\text{N}_2$  most strongly interacted with  $\text{GR(37)-Li/Li}^+$ , followed by  $\text{O}_2$ , and Ar.

#### 4.7.1. Effects of GR(37) to Binding of Ar/ $\text{N}_2/\text{O}_2$ to Li/ $\text{Li}^+$

As mentioned in Section 4.5.,  $\text{Li/Li}^+$  always had about 1 charge so  $\text{Li}^+-\text{A}_n$  was compared with  $\text{GR(37)-Li/Li}^+-\text{A}_n$ , with respect to energy parameters. In Figure 19, plots of  $\text{Li}^+$  was similar to  $\text{GR(37)-Li/Li}^+$ , but GR(37) weakened all the binding energy so it is obvious that GR(37) is detrimental to binding of air molecules to  $\text{Li}^+$ .

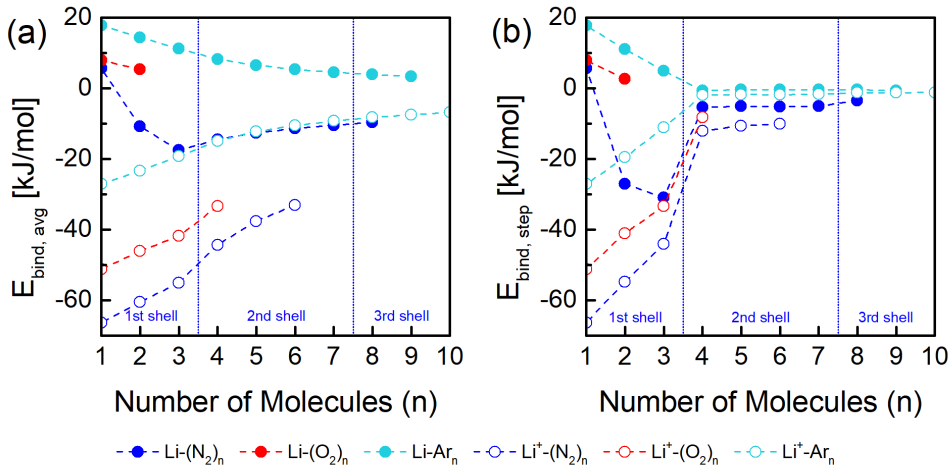


**Figure 20.** (a) Average and (b) stepwise binding energy of Ar,  $\text{N}_2$ , and  $\text{O}_2$  to Li and  $\text{Li}^+$ . All computational works were performed by UCAM-B3LYP/6-311G(d,p) level.

Figure 20 shows (a) average and (b) stepwise binding energy of  $\text{Li/Li}^+-\text{A}_n$ . Unlike  $\text{GR(37)-Li/Li}^+-\text{A}_n$ , the plots of neutral and positive system in Figure 20 were much different from each other. The binding energy of Li was weaker or even endothermic, so the binding was more unfavorable than  $\text{Li}^+$ . Overall,  $\text{Li}^+$  had the strongest

interaction, followed by GR(37)–Li/Li<sup>+</sup>, and Li.

Therefore, it was clarified that the role of GR(37) is stabilization of the charge of Li/Li<sup>+</sup> to about 1, as revealed in Section 4.5., and maintaining the exothermicity of binding energy. To sum up, GR(37) maintained the binding environment of Li/Li<sup>+</sup> similar as Li<sup>+</sup>.

#### 4.8. Stability of GR(37)–Li/Li<sup>+</sup>–A<sub>n</sub>

The stability of the binding structures was determined from the frequency calculations. For GR(37)–Li/Li<sup>+</sup>–(N<sub>2</sub>)<sub>n</sub>, GR(37)–Li<sup>+</sup>–(N<sub>2</sub>)<sub>6</sub> possessed an imaginary frequency at  $-910.82\text{ cm}^{-1}$  with twisting of hexagonal rings of GR(37), implying the breaking of sp<sup>2</sup> hybridization of C to sp<sup>3</sup>, whereas the neutral system was stable until the next shell. For GR(37)–Li/Li<sup>+</sup>–(O<sub>2</sub>)<sub>n</sub>, GR(37)–Li–(O<sub>2</sub>)<sub>2</sub> possessed an imaginary frequency at  $-1.53\text{ cm}^{-1}$  with flapping of +y and -y parts of GR(37) to +z and -z direction simultaneously, implying the exfoliation of the GR(37), whereas the positive system was stable until the next shell. On the other hand, no imaginary frequency was found from GR(37)–Li/Li<sup>+</sup>–Ar<sub>n</sub>.<sup>⑤</sup>

Therefore, it is sure that excess N<sub>2</sub> or O<sub>2</sub> can damage the GR(37), but such negative effects were not found in Ar clusters.

#### 4.9. Effects of Dispersion Corrections

To apply the dispersions, GR(37)–Li<sup>+</sup>–Ar<sub>3</sub>, GR(37)–Li<sup>+</sup>–(N<sub>2</sub>)<sub>3</sub>, and GR(37)–Li<sup>+</sup>–(O<sub>2</sub>)<sub>3</sub> were chosen to represent the direct interaction,

---

<sup>⑤</sup> The stability of Ar clusters could be evaluated by the average kinetic energy of gas molecules at 298.15 K,

$$\frac{3}{2}k_B T = 3.718 \text{ kJ/mol} \quad (4.3)$$

where  $k_B$  and  $T$  are the Boltzmann constant and temperature, respectively.<sup>53</sup> If the binding energy is endothermic than  $-3.718\text{ kJ/mol}$ , then a collision of gas molecule will easily detach the bound molecule. From this point of view, in room temperature, the cluster could grow until GR(37)–Li–Ar<sub>7</sub> and GR(37)–Li<sup>+</sup>–Ar<sub>9</sub>, in terms of the average binding energy. However, according to the stepwise binding energy, the structures would evolve until GR(37)–Li–Ar<sub>2</sub> and GR(37)–Li<sup>+</sup>–Ar<sub>3</sub>.

and  $\text{GR}(37)-\text{Li}^+-\text{Ar}_{10}$ ,  $\text{GR}(37)-\text{Li}^+-\text{(N}_2)_6$ , and  $\text{GR}(37)-\text{Li}^+-\text{(O}_2)_4$  were chosen to represent the maximum binding structure. These two groups were compared to check the effects on the indirect interaction.

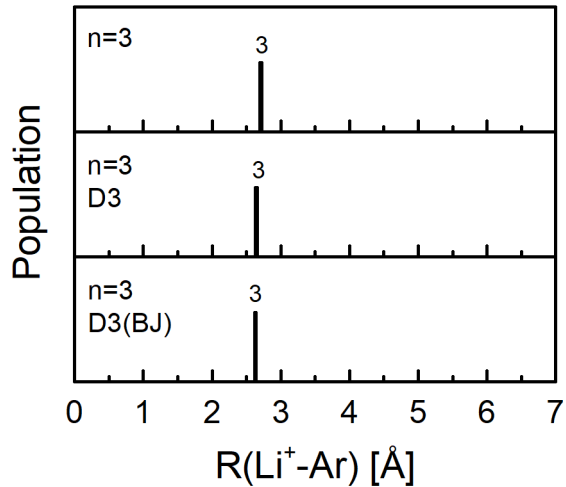


**Figure 21.** Stick diagrams of  $R(\text{Li}^+ - \text{Ar})$  from  $\text{GR}(37)-\text{Li}^+-\text{Ar}_3$  by computations with UCAM-B3LYP/6-311G(d,p) level and various dispersions. Above the sticks, the degeneracy of binding is denoted.

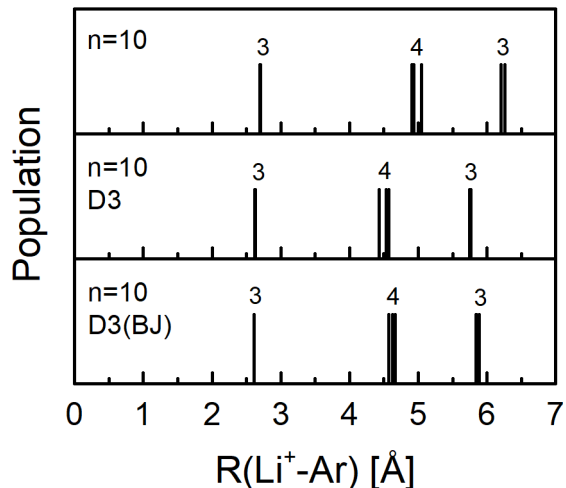


**Figure 22.** Stick diagrams of  $R(\text{Li}^+ - \text{Ar})$  from  $\text{GR}(37)-\text{Li}^+-\text{Ar}_{10}$  by computations with UCAM-B3LYP/6-311G(d,p) level and various dispersions. Above the sticks, the degeneracy of binding is denoted.

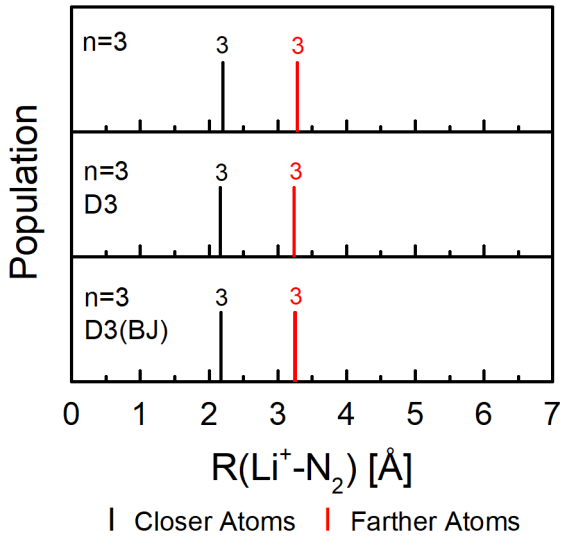


**Figure 23.** Stick diagrams of  $R(\text{Li}^+ - \text{N}_2)$  from GR(37)– $\text{Li}^+-(\text{N}_2)_3$  by computations with UCAM–B3LYP/6–311G(d,p) level and various dispersions. Above the sticks, the degeneracy of binding is denoted.

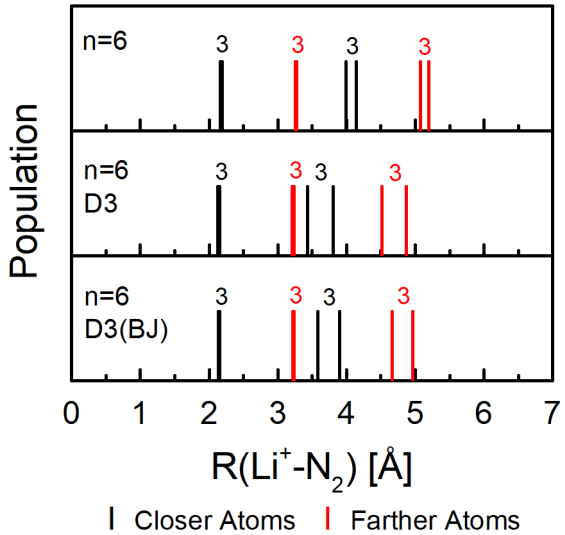


**Figure 24.** Stick diagrams of  $R(\text{Li}^+ - \text{N}_2)$  from GR(37)– $\text{Li}^+-(\text{N}_2)_6$  by computations with UCAM–B3LYP/6–311G(d,p) level and various dispersions. Above the sticks, the degeneracy of binding is denoted.

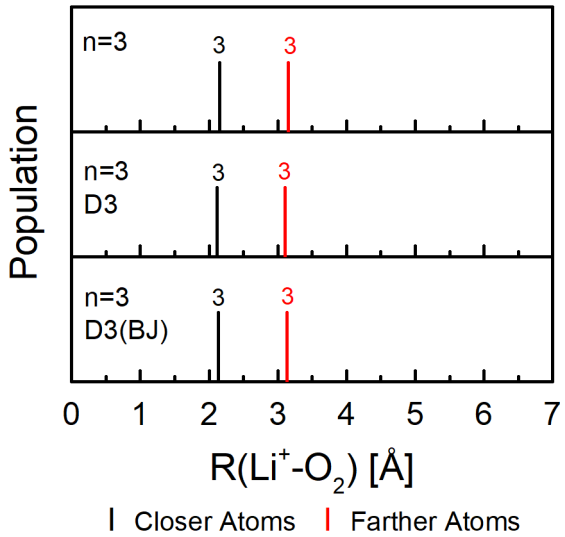


**Figure 25.** Stick diagrams of  $R(\text{Li}^+ - \text{O}_2)$  from GR(37)– $\text{Li}^+-(\text{O}_2)_3$  by computations with UCAM–B3LYP/6–311G(d,p) level and various dispersions. Above the sticks, the degeneracy of binding is denoted.

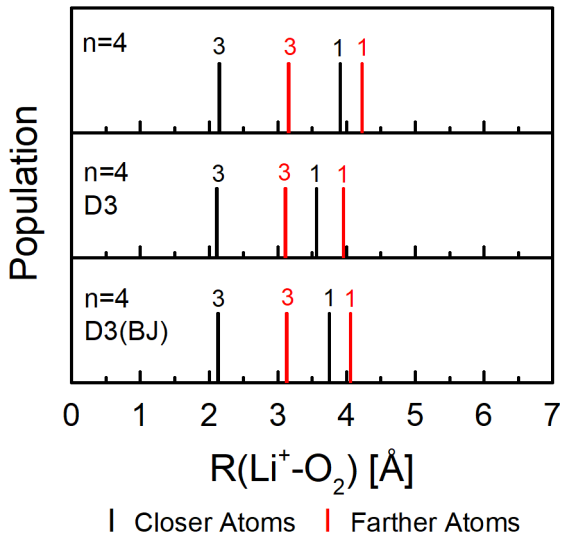


**Figure 26.** Stick diagrams of  $R(\text{Li}^+ - \text{O}_2)$  from GR(37)– $\text{Li}^+-(\text{O}_2)_4$  by computations with UCAM–B3LYP/6–311G(d,p) level and various dispersions. Above the sticks, the degeneracy of binding is denoted.

Figure 21–26 show the stick diagrams of the binding distance between  $\text{Li}^+$  and Ar,  $\text{N}_2$ , and  $\text{O}_2$  with various dispersion corrections. The innermost three directly binding molecules were subtly affected by the dispersions, whereas additional molecules showed evident shortening of the distance.

**Table 2.** Charge of the  $\text{Li}^+$  Calculated at the UCAM–B3LYP/6–311G(d,p) Level with the Various Dispersions

System	–	D3	D3(BJ)
GR(37)– $\text{Li}^+$	0.976	0.976	0.976
GR(37)– $\text{Li}^+$ – $\text{Ar}_3$	0.887	0.876	0.875
GR(37)– $\text{Li}^+$ – $\text{Ar}_{10}$	0.882	0.869	0.869
GR(37)– $\text{Li}^+$ –( $\text{N}_2$ ) <sub>3</sub>	0.817	0.811	0.810
GR(37)– $\text{Li}^+$ –( $\text{N}_2$ ) <sub>6</sub>	0.797	0.783	0.785
GR(37)– $\text{Li}^+$ –( $\text{O}_2$ ) <sub>3</sub>	0.862	0.856	0.858
GR(37)– $\text{Li}^+$ –( $\text{O}_2$ ) <sub>4</sub>	0.856	0.849	0.851

**Table 3.** Charge of the Central Ring of the GR(37) Calculated at the UCAM–B3LYP/6–311G(d,p) Level with the Various Dispersions

System	–	D3	D3(BJ)
GR(37)– $\text{Li}^+$	–0.477	–0.480	–0.480
GR(37)– $\text{Li}^+$ – $\text{Ar}_3$	–0.426	–0.426	–0.423
GR(37)– $\text{Li}^+$ – $\text{Ar}_{10}$	–0.421	–0.417	–0.416
GR(37)– $\text{Li}^+$ –( $\text{N}_2$ ) <sub>3</sub>	–0.351	–0.345	–0.351
GR(37)– $\text{Li}^+$ –( $\text{N}_2$ ) <sub>6</sub>	–0.332	–0.311	–0.317
GR(37)– $\text{Li}^+$ –( $\text{O}_2$ ) <sub>3</sub>	–0.381	–0.375	–0.377
GR(37)– $\text{Li}^+$ –( $\text{O}_2$ ) <sub>4</sub>	–0.379	–0.367	–0.373

Table 2 and 3 show the charge of the  $\text{Li}^+$  and the central ring of the GR(37), respectively, with various dispersion corrections. Regardless of the corrections, the computations resulted in similar charge values to the same system. The corrected charge tendencies were analogous to the aspects of Section 4.5.

**Table 4.** Height of the  $\text{Li}^+$  from the GR(37) ( $\text{\AA}$ ) Calculated at the UCAM–B3LYP/6–311G(d,p) Level with the Various Dispersions

System	–	D3	D3(BJ)
GR(37)– $\text{Li}^+$	1.771	1.770	1.765
GR(37)– $\text{Li}^+$ – $\text{Ar}_3$	1.856	1.818	1.839
GR(37)– $\text{Li}^+$ – $\text{Ar}_{10}$	1.868	1.843	1.851
GR(37)– $\text{Li}^+$ – $(\text{N}_2)_3$	1.994	1.983	1.948
GR(37)– $\text{Li}^+$ – $(\text{N}_2)_6$	2.044	2.082	2.056
GR(37)– $\text{Li}^+$ – $(\text{O}_2)_3$	1.921	1.909	1.904
GR(37)– $\text{Li}^+$ – $(\text{O}_2)_4$	1.928	1.927	1.914

Table 4 shows the height of the  $\text{Li}^+$  from the GR(37) with various dispersion corrections. The height values and its tendencies were marginally affected by the corrections because the influence of the dispersion corrections to the charge of the binding system was weak.

**Table 5.** Average Binding Energy of Ar,  $\text{N}_2$ , and  $\text{O}_2$  to the  $\text{Li}^+$  (kJ/mol) Calculated at the UCAM–B3LYP/6–311G(d,p) Level with the Various Dispersions

System	–	D3	D3(BJ)
GR(37)– $\text{Li}^+$ – $\text{Ar}_3$	–8.776	–20.491	–21.449
GR(37)– $\text{Li}^+$ – $\text{Ar}_{10}$	–3.544	–12.668	–13.225
GR(37)– $\text{Li}^+$ – $(\text{N}_2)_3$	–34.489	–48.571	–49.486
GR(37)– $\text{Li}^+$ – $(\text{N}_2)_6$	–21.824	–35.302	–35.999
GR(37)– $\text{Li}^+$ – $(\text{O}_2)_3$	–28.667	–42.221	–40.506
GR(37)– $\text{Li}^+$ – $(\text{O}_2)_4$	–23.283	–35.058	–33.447

Table 5 shows the average binding energy of Ar,  $\text{N}_2$ , and  $\text{O}_2$  to the  $\text{Li}^+$  with various dispersion corrections. Noticeable increase of the exothermicity of the average binding energy about 10 kJ/mol was observed. The corrected average binding energy tendencies were analogous to the aspects of Section 4.7.

Overall, the effects of the dispersion corrections were feeble at

the vicinity of ionically charged place and strong at interaction of the air molecules. Qualitative tendencies of the binding were analogous to the results without the corrections. However, quantitative parameters showed the glaring differences by UCAM-B3LYP-D3 and UCAM-B3LYP-D3(BJ).

## Chapter 5. Discussion

### 5.1. Comparison with Previous Study on H<sub>2</sub>

The general trend of previous study on H<sub>2</sub> by Tachikawa and Iyama<sup>12</sup> was in accord with the trend in this work. However, several distinct features were found.

First, H<sub>2</sub> was bound with a side-on structure, and it was analogous to nonclassical 2-electron 3-center bond.<sup>54</sup> Due to the side-on orientation, dissipation of its symmetry was more obvious than O<sub>2</sub>. Second, without the dispersions, the order of the average binding energy was Ar < H<sub>2</sub> < O<sub>2</sub> < N<sub>2</sub>.

### 5.2. Additional Comments

**Table 6.** Charge of Li/Li<sup>+</sup> of GR(37)–Li/Li<sup>+</sup> Calculated at the UCAM–B3LYP/6–311G(d,p) Level

Origin	Li of GR(37)–Li	Li <sup>+</sup> of GR(37)–Li <sup>+</sup>
Previous Reports <sup>9, 12</sup>	0.929	0.936
In This Work	0.973	0.976

Table 6 shows the charge of previous reports and this work. Like the discrepancy in Table 6, in this study, the charges for  $n = 0$  were not agreed with previous work, even though the structures were well reproduced as mentioned in Section 4.1.

The coordination number of Li/Li<sup>+</sup> was not considered in this study. It might be the reason of difference in binding property between Li and Mg.<sup>13</sup>

In addition, this study has simplified the real ambient air. In fact, air is mixture of not only N<sub>2</sub>, O<sub>2</sub>, and Ar, but also other minor compounds like H<sub>2</sub>O. The interaction among different molecules and the effect of the minor compounds were not simulated in this study.

## Chapter 6. Conclusions

In this study, the effect of air molecules to GR(37)–Li/Li<sup>+</sup> was investigated by DFT method. The results were compared with previous study on H<sub>2</sub>.

The doping of Li/Li<sup>+</sup> enhanced the binding strength of Ar and N<sub>2</sub> as well as H<sub>2</sub> and achieved the binding of O<sub>2</sub> onto GR(37) surface. In this process, the spin state of O<sub>2</sub> was verified as triplet. Shell structure was built during the binding of the molecules. Three innermost molecules composed the first shell, and these molecules and Li/Li<sup>+</sup> directly interacted. Additional four molecules composed the second shell, and the third shell was confirmed. The binding in these outer two shells was indirect. Various binding structures and orientational effects were confirmed from no orientational effect of Ar, linear end-on structure of N<sub>2</sub>, bent end-on structure of O<sub>2</sub>, and side-on structure of H<sub>2</sub>. In all the systems, the charge of Li/Li<sup>+</sup> was about 1, and binding energy was exothermic, because of GR(37). The order of the average binding energy was Ar < H<sub>2</sub> < O<sub>2</sub> < N<sub>2</sub>. The growth of the binding systems was limited by the imaginary frequency for N<sub>2</sub> and O<sub>2</sub>. The dispersion corrections could be applied to analyze in detail about interaction of air molecules.

From these results, we can infer two realistic results. First, for H<sub>2</sub> storage, the binding of N<sub>2</sub> and O<sub>2</sub> onto GR(37)–Li/Li<sup>+</sup> is stronger than H<sub>2</sub>, so exposure of GR(37)–Li/Li<sup>+</sup> to air can lower the H<sub>2</sub> storage capacity. Second, for Li–air battery, due to the accompanied imaginary frequency, excess N<sub>2</sub> or O<sub>2</sub> can damage Li doped graphene electrode.

## Bibliography

1. Atkins, P. W.; De Paula, J.; Keeler, J. *Atkins' Physical Chemistry*, 11th ed.; Oxford University Press, 2018.
2. Foresman, J. B.; Frisch, A. E. *Exploring Chemistry with Electronic Structure Methods*, 3rd ed.; Gaussian, Inc.: Wallingford, CT, 2015.
3. Novoselov, K. S.; Geim, A. K.; Morozov, S. V.; Jiang, D.; Zhang, Y.; Dubonos, S. V.; Grigorieva, I. V.; Firsov, A. A. Electric Field Effect in Atomically Thin Carbon Films. *Science* **2004**, *306*, 666–669.
4. Su, C.; Tripathi, M.; Yan, Q.-B.; Wang, Z.; Zhang, Z.; Hofer, C.; Wang, H.; Basile, L.; Su, G.; Dong, M.; et al. Engineering Single-Atom Dynamics with Electron Irradiation. *Sci. Adv.* **2019**, *5*.
5. Bao, Q.; Loh, K. P. Graphene Photonics, Plasmonics, and Broadband Optoelectronic Devices. *ACS Nano* **2012**, *6*, 3677–3694.
6. Pei, S.; Cheng, H.-M. The Reduction of Graphene Oxide. *Carbon* **2012**, *50*, 3210–3228.
7. Kheirabadi, N.; Shafiekhani, A. Graphene/Li–Ion Battery. *J. Appl. Phys.* **2012**, *112*, 124323.
8. Sakaushi, K.; Antonietti, M. Carbon– and Nitrogen–Based Organic Frameworks. *Acc. Chem. Res.* **2015**, *48*, 1591–1600.
9. Tachikawa, H. Mechanism of Li Storage on Graphene Nanoflakes: Density Functional Theory Study. *Surf. Sci.* **2020**, *691*, 121489.
10. Mo, R.; Tan, X.; Li, F.; Tao, R.; Xu, J.; Kong, D.; Wang, Z.; Xu, B.; Wang, X.; Wang, C.; et al. Tin–Graphene Tubes as Anodes for Lithium–Ion Batteries with High Volumetric and Gravimetric Energy Densities. *Nat. Commun.* **2020**, *11*, 1374.
11. Gu, J.; Zhang, X.; Fu, L.; Pang, A. Study on the Hydrogen Storage Properties of the Dual Active Metals Ni and Al Doped Graphene Composites. *Int. J. Hydrogen Energy* **2019**, *44*, 6036–6044.
12. Tachikawa, H.; Iyama, T. Mechanism of Hydrogen Storage in the Graphene Nanoflake–Lithium–H<sub>2</sub> System. *J. Phys. Chem. C* **2019**,

123, 8709–8716.

13. Tachikawa, H.; Izumi, Y.; Iyama, T.; Azumi, K. Molecular Design of a Reversible Hydrogen Storage Device Composed of the Graphene Nanoflake–Magnesium–H<sub>2</sub> System. *ACS Omega* **2021**, *6*, 7778–7785.
14. Girishkumar, G.; McCloskey, B.; Luntz, A. C.; Swanson, S.; Wilcke, W. Lithium–Air Battery: Promise and Challenges. *J. Phys. Chem. Lett.* **2010**, *1*, 2193–2203.
15. Wang, C.; Xie, Z.; Zhou, Z. Lithium–Air Batteries: Challenges Coexist with Opportunities. *APL Mater.* **2019**, *7*, 040701.
16. Lu, J.; Jung Lee, Y.; Luo, X.; Chun Lau, K.; Asadi, M.; Wang, H.–H.; Brombosz, S.; Wen, J.; Zhai, D.; Chen, Z.; et al. A Lithium–Oxygen Battery Based on Lithium Superoxide. *Nature* **2016**, *529*, 377–382.
17. Ma, J.–L.; Bao, D.; Shi, M.–M.; Yan, J.–M.; Zhang, X.–B. Reversible Nitrogen Fixation Based on a Rechargeable Lithium–Nitrogen Battery for Energy Storage. *Chem* **2017**, *2*, 525–532.
18. Lee, J. H.; Kang, S. G.; Kim, I. T.; Kwon, S.; Lee, I.; Lee, S. G. Adsorption Mechanisms of Lithium Oxides (Li<sub>x</sub>O<sub>2</sub>) on N–Doped Graphene: A Density Functional Theory Study with Implications for Lithium–Air Batteries. *Theor. Chem. Acc.* **2016**, *135*, 50.
19. Levine, I. N. *Quantum Chemistry*, 7th ed.; Pearson, 2014.
20. Moon, H.–W. Hydrogen Storage in Graphene Oxide Layers: First–Principles Study and Monte Carlo Simulations. Master thesis, Seoul National University, Seoul, 2015.
21. Vuckovic, S.; Song, S.; Kozlowski, J.; Sim, E.; Burke, K. Density Functional Analysis: The Theory of Density–Corrected DFT. *J. Chem. Theory Comput.* **2019**, *15*, 6636–6646.
22. Mahmood, J.; Lee, E. K.; Jung, M.; Shin, D.; Jeon, I.–Y.; Jung, S.–M.; Choi, H.–J.; Seo, J.–M.; Bae, S.–Y.; Sohn, S.–D.; et al. Nitrogenated Holey Two–Dimensional Structures. *Nat. Commun.* **2015**, *6*, 6486.
23. Orellana, W. Catalytic Properties of Transition Metal–N<sub>4</sub> Moieties in Graphene for the Oxygen Reduction Reaction: Evidence of Spin–Dependent Mechanisms. *J. Phys. Chem. C* **2013**, *117*,

9812–9818.

24. Seekaew, Y.; Wongchoosuk, C. A Novel Graphene-Based Electroluminescent Gas Sensor for Carbon Dioxide Detection. *Appl. Surf. Sci.* **2019**, *479*, 525–531.
25. Impeng, S.; Junkaew, A.; Maitarad, P.; Kungwan, N.; Zhang, D.; Shi, L.; Namuangruk, S. A MnN<sub>4</sub> Moiety Embedded Graphene as a Magnetic Gas Sensor for CO Detection: A First Principle Study. *Appl. Surf. Sci.* **2019**, *473*, 820–827.
26. Sendt, K.; Haynes, B. S. Density Functional Study of the Chemisorption of O<sub>2</sub> across Two Rings of the Armchair Surface of Graphite. *J. Phys. Chem. C* **2007**, *111*, 5465–5473.
27. Chouhan, R. K.; Ulman, K.; Narasimhan, S. Graphene Oxide as an Optimal Candidate Material for Methane Storage. *J. Chem. Phys.* **2015**, *143*, 044704.
28. Burganova, R.; Lysogorskiy, Y.; Nedopekin, O.; Tayurskii, D. Adsorption of Helium Atoms on Two-Dimensional Substrates. *J. Low Temp. Phys.* **2016**, *185*, 392–398.
29. Sahoo, S. K.; Heske, J.; Azadi, S.; Zhang, Z.; Tarakina, Nadezda V.; Oschatz, M.; Khaliullin, R. Z.; Antonietti, M.; Kühne, T. D. On the Possibility of Helium Adsorption in Nitrogen Doped Graphitic Materials. *Sci. Rep.* **2020**, *10*, 5832.
30. Chen, C.; Kong, W.; Duan, H.; Zhang, J. Theoretical Simulation of the Reduction of Graphene Oxide by Lithium Naphthalenide. *Phys. Chem. Chem. Phys.* **2015**, *17*, 13654–13658.
31. Tachikawa, H. Hydrogen Atom Addition to the Surface of Graphene Nanoflakes: A Density Functional Theory Study. *Appl. Surf. Sci.* **2017**, *396*, 1335–1342.
32. Tachikawa, H.; Kawabata, H. Additions of Fluorine Atoms to the Surfaces of Graphene Nanoflakes: A Density Functional Theory Study. *Solid State Sci.* **2019**, *97*, 106007.
33. Widjaja, H.; Jiang, Z.-T.; Altarawneh, M.; Yin, C.-Y.; Goh, B.-M.; Mondinos, N.; Dlugogorski, B. Z. Towards a Better Understanding of the Geometrical and Orientational Aspects of the Electronic Structure of Halogens (F–I) Adsorption on

- Graphene. *Appl. Surf. Sci.* **2015**, *356*, 370–377.
- 34. Zhao, W.-H.; Yang, L.-J.; Qing, L.-H.; Lv, X.-M.; Yi, L.-Y.; Li, H.; Chen, Z.-Q. The Strong Effect of Substituents on the Carbonyl Reduction in Graphene Oxide: A DFT Study. *Comput. Theor. Chem.* **2015**, *1068*, 1–7.
  - 35. Guo, J.; Lee, J.; Contescu, C. I.; Gallego, N. C.; Pantelides, S. T.; Pennycook, S. J.; Moyer, B. A.; Chisholm, M. F. Crown Ethers in Graphene. *Nat. Commun.* **2014**, *5*, 5389.
  - 36. Jiang, Q. G.; Ao, Z. M.; Jiang, Q. First Principles Study on the Hydrophilic and Conductive Graphene Doped with Al Atoms. *Phys. Chem. Chem. Phys.* **2013**, *15*, 10859–10865.
  - 37. Guan, S.; Cheng, Y.; Liu, C.; Han, J.; Lu, Y.; Yang, S. A.; Yao, Y. Effects of Strain on Electronic and Optic Properties of Holey Two-Dimensional C<sub>2</sub>N Crystals. *Appl. Phys. Lett.* **2015**, *107*, 231904.
  - 38. Yao, Q.; Huang, C.; Yuan, Y.; Liu, Y.; Liu, S.; Deng, K.; Kan, E. Theoretical Prediction of Phosphorene and Nanoribbons as Fast-Charging Li Ion Battery Anode Materials. *J. Phys. Chem. C* **2015**, *119*, 6923–6928.
  - 39. Tang, Q.; Zhou, Z.; Chen, Z. Innovation and Discovery of Graphene-Like Materials Via Density-Functional Theory Computations. *WIREs Comput. Mol. Sci.* **2015**, *5*, 360–379.
  - 40. Bryantsev, V. S.; Blanco, M.; Faglioni, F. Stability of Lithium Superoxide LiO<sub>2</sub> in the Gas Phase: Computational Study of Dimerization and Disproportionation Reactions. *J. Phys. Chem. A* **2010**, *114*, 8165–8169.
  - 41. Lente, G. Facts and Alternative Facts in Chemical Kinetics: Remarks About the Kinetic Use of Activities, Termolecular Processes, and Linearization Techniques. *Curr. Opin. Chem. Eng.* **2018**, *21*, 76–83.
  - 42. Frisch, M. J.; Trucks, G. W.; Schlegel, H. B.; Scuseria, G. E.; Robb, M. A.; Cheeseman, J. R.; Scalmani, G.; Barone, V.; Petersson, G. A.; Nakatsuji, H.; et al. *Gaussian 16*, Revision A.03, Gaussian, Inc., Wallingford, CT, 2016.
  - 43. Yanai, T.; Tew, D. P.; Handy, N. C. A New Hybrid Exchange-

Correlation Functional Using the Coulomb–Attenuating Method (CAM–B3LYP). *Chem. Phys. Lett.* **2004**, *393*, 51–57.

44. McLean, A. D.; Chandler, G. S. Contracted Gaussian Basis Sets for Molecular Calculations. I. Second Row Atoms, Z=11–18. *J. Chem. Phys.* **1980**, *72*, 5639–5648.
45. Foster, J. P.; Weinhold, F. Natural Hybrid Orbitals. *J. Am. Chem. Soc.* **1980**, *102*, 7211–7218.
46. Grimme, S.; Antony, J.; Ehrlich, S.; Krieg, H. A Consistent and Accurate Ab Initio Parametrization of Density Functional Dispersion Correction (DFT–D) for the 94 Elements H–Pu. *J. Chem. Phys.* **2010**, *132*, 154104.
47. Grimme, S.; Ehrlich, S.; Goerigk, L. Effect of the Damping Function in Dispersion Corrected Density Functional Theory. *J. Comput. Chem.* **2011**, *32*, 1456–1465.
48. Dan, Y.; Lu, Y.; Kybert, N. J.; Luo, Z.; Johnson, A. T. C. Intrinsic Response of Graphene Vapor Sensors. *Nano Lett.* **2009**, *9*, 1472–1475.
49. Lindsay, D. M.; Garland, D. A. ESR Spectra of Matrix–Isolated Lithium Superoxide. *J. Phys. Chem.* **1987**, *91*, 6158–6161.
50. Stephen, J. L.; Berg, J. M. *Principles of Bioinorganic Chemistry*; University Science Books, 1994.
51. Fayer, M. D.; Levinger, N. E. Analysis of Water in Confined Geometries and at Interfaces. *Annu. Rev. Anal. Chem.* **2010**, *3*, 89–107.
52. Allen, A. D.; Senoff, C. V. Nitrogenopentammineruthenium(II) Complexes. *Chem. Commun. (London)* **1965**, 621–622.
53. Halliday, D.; Walker, J.; Resnick, R. *Halliday and Resnick' s Principles of Physics*, 11th ed.; John Wiley & Sons, Limited, 2020.
54. Kubas, G. J. Fundamentals of H<sub>2</sub> Binding and Reactivity on Transition Metals Underlying Hydrogenase Function and H<sub>2</sub> Production and Storage. *Chem. Rev.* **2007**, *107*, 4152–4205.

# 초 록

## 밀도범함수 이론을 통한 그래핀 나노플레이크에서의 공기 구성 분자와 리튬의 상호작용 연구

서울대학교 대학원  
화학부 물리화학 전공  
신채수

그래핀의 출현은 2010년 노벨물리학상을 수상한 대단히 영향력 있는 사건이었으며, 이를 전자소재, 광 소재, 신물질, 2차원 표면화학 등에 폭넓게 응용하는 데에 대단한 주목이 있었다. 이에 대한 주요한 관심의 하나로 그래핀과 다른 화학물질의 표면상호작용을 토대로 하는 촉매 작용, 센서, 물질 저장이 있다. 특히 Li이 도핑된 그래핀은 Li 저장, H<sub>2</sub> 저장, 리튬-공기 배터리 등의 다양한 에너지 용도의 저장 소재와 관련이 있다. 이러한 목적을 실용적으로 이루려면, 공기 분자들이 그래핀-Li 시스템에 미치는 영향을 평가하는 것이 필수적이다.

화학적 관점에서는, 그래핀 및 그래핀 유사물질의 성질 및 응용을 탐구하기 위해 계산적 접근이 이루어졌다. 이러한 이론적 연구는 밀도범함수 이론을 폭넓게 이용하였으며, 그래핀의 표면 및 모서리, 독특한 그래핀 유사물질, 에너지 저장에의 응용 등 다양한 시스템의 연구에 적용되었다. 특히, 리튬-공기 배터리는 직접적인 시뮬레이션 대상이 되기도 하였으나, 공기와의 상호작용은 아직 완전히 주목받지 못하였다.

이 학위논문에서는 공기 분자들과 Li/Li<sup>+</sup>의 그래핀 나노플레이크 상에서의 상호작용 및 그 특징을 밝히기 위한 연구가 밀도범함수 이론을 통해 진행되었다. 챕터 1에 이러한 연구의 동기 및 필요성이 제시되었다. 챕터 2에서 관련 배경지식이 소개되었으며, 특히 밀도범함수 이론에 관한 계산화학 및 그래핀에 대한 내용을 다뤘다. 이전의 그래핀의 성질 및 응용에 대한 연구, 그래핀에 대한 계산상 연구도 논의되었다.

챕터 3에서, 이 연구에서의 계산상 방법들이 자세히 나타나 있으며, 챕터 4에서는, 이 계산의 결과가 설명되었다. Li/Li<sup>+</sup>의 역할은 Ar, N<sub>2</sub>,

$O_2$ 의 결합을 구현하는 것이었으며, 이때  $O_2$ 의 스픈은 삼중항이었다. 공기 분자들의 결합 구조는 용액에서 나타나는 용매의 껍질 구조와 유사하였고, 특히 공기 분자와  $Li/Li^+$ 는 첫 번째 껍질에서만 직접적으로 상호 작용하였다. Ar과 다르게  $N_2$ 와  $O_2$ 는 직선형 말단결합구조와 굽은형 말단결합구조를 각각 보였으며, 배향 효과 역시 나타났다.  $Li/Li^+$ 의 전하는 항상 거의 1이었으며, 이것으로 중성 시스템에서의 전하 이동을 알 수 있었다. 평균 결합 에너지는 수렴하는 경향을 보였으며, 단계적 결합 에너지가 두 번째 및 세 번째 껍질에서는 거의 작은 값으로 일정한 것이 그 원인이었다. 불안정한 음의 진동수를 기준으로 하였을 때 결합 구조의 성장은 제한될 수밖에 없었다. 분산 효과는 기체 분자의 상호작용에서 두드리지게 나타났다.

챕터 5에서, 결과에 대한 논의가 제시되었으며  $H_2$ 와의 비교 및 몇몇 짚을 점들이 포함되었다. 마지막으로, 챕터 6에서는 연구의 결론이 제시되었다. 이 연구로부터, 공기는  $H_2$  저장능력을 약화시킬 수 있다는 것을 알게 되었다. 또한, Li이 도핑된 그래핀 전극은 과량의  $N_2$  및  $O_2$ 에 의해 손상될 수 있었다.

**주요어 :** 밀도범함수 이론, 그래핀, 그래핀 나노플레이크, 리튬, 공기, 주위 환경

**학 번 :** 2015-20388

## 감사의 말

학위를 위한 연구 과정에서 막혔을 때마다 나와 직접적인 토의의 대상으로 헌신한 김민우, 손문기, 신동한, Tony Cho에게 감사함을 전합니다. 그 동안 나의 삶에 직/간접적으로 긍정적 영향을 주었던 수많은 이들에게도 고맙습니다.